Cation-disordered rocksalt-type high-entropy cathodes for Li-ion batteries

Zhengyan Lun [†ab], Bin Ouyang [†ab], Deok-Hwang Kwon [ab], Yang Ha [c], Emily E. Foley [d], Tzu-Yang Huang [eg], Zijian Cai [ab], Hyunchul Kim [b], Mahalingam Balasubramanian [f], Yingzhi Sun [ab], Jianping Huang [b], Yaosen Tian [ab], Haegyeom Kim [b], Bryan D. McCloskey [eg], Wanli Yang [c], Raphaële J. Clément [d], Huiwen Ji [g*], Gerbrand Ceder [ab*]

[a] Department of Materials Science and Engineering, UC Berkeley, Berkeley, CA 94720, USA

[b] Materials Sciences Division, LBNL, Berkeley, CA 94720, USA

[c] Advanced Light Source, Lawrence Berkeley National Laboratory, Berkeley, CA 94720, USA

[d] Materials Department, University of California, Santa Barbara, CA 93106, USA

[e] Department of Chemical and Biomolecular Engineering, UC Berkeley, Berkeley, CA 94720, USA

[f] X-ray Science Division, Advanced Photon Source, Argonne National Laboratory, Argonne, IL 60439, USA

[g] Energy Storage and Distributed Resources Division, LBNL, Berkeley, CA 94720, USA

[†] These authors contributed equally.

[*] email: huiwenji@lbl.gov, gceder@berkeley.edu

Summary

High-entropy (HE) ceramics, by analogy with high-entropy metallic alloys, are an emerging class of solid solutions composed of a large number of species. These materials offer the benefit of large compositional flexibility and can be used in a wide variety of applications, including thermoelectrics, catalysts, superionic conductors and battery electrodes. We show in this paper that the HE-concept can lead to very significant improvements in performance in battery cathodes. Among lithium (Li)-ion cathodes, cation-disordered rocksalt (DRX)-type materials are an ideal platform within which to design HE materials because of their demonstrated chemical flexibility. By comparing a group of DRX cathodes containing two, four or six transition metal (TM) species, we show that short-range order (SRO) systematically decreases while energy density and rate capability systematically increase as more TM cation species are mixed together, even though the total metal content remains fixed. A DRX cathode with six TM species achieves 307 mAh g^{-1} (955 Wh kg^{-1}) at a low rate (20 mA g^{-1}), and retains more than 170 mAh g^{-1} when cycling at a high rate of 2,000 mA g^{-1}. To facilitate further design in this HE DRX space, we also present a compatibility analysis of twenty-three different TM ions, and successfully synthesize a phase-pure HE DRX compound containing twelve TM species, as a proof-of-concept.

Main

Emerging in the field of metallic alloys [1,2] is the concept of high-entropy (HE) materials, which combine multiple principal elements to create new single-phase materials [3,4]. Over the past few years, the 'HE strategy' has been applied across various fields, including thermoelectricity [5], catalysis [6], superionic conductivity [7] and energy storage [8,9,10]. The large configurational entropy is believed to enhance the simultaneous solubility of a large number of components, which can then be selected to optimize target properties. In recent studies on the atomic-scale structure of HE compounds, including $(V_{0.2}Nb_{0.2}Ta_{0.2}Mo_{0.2}W_{0.2})C$ [11] and $(Mg_{0.2}Co_{0.2}Ni_{0.2}Cu_{0.2}Zn_{0.2})O$[12], a uniform distribution of different transition metals (TMs) was observed, indicating the capability of suppressing cation short-range order (SRO) by mixing together a large number of TM species.

The concept of HE in lithium (Li)-ion electrode materials, if successfully implemented, can be highly attractive as it facilitates the simultaneous optimization of multiple properties. In addition, compositional flexibility would alleviate the industry's reliance on any single critical metal source. The recently-developed cation-disordered rocksalt (DRX) cathodes [13-15], in which Li migrates through a percolating network of 0-TM clusters without TM coordination around the activated state, are ideal targets for such HE designs. In DRX cathodes, significant SRO has been observed, which directly degrades long-range Li transport [16-19]. Monte Carlo simulations[16] have shown that the presence of SRO in DRX cathodes generally leads to reduced Li percolation, when compared to that of a random arrangement of metal species. In addition, DRX structures have a large compositional flexibility and can incorporate many TM species[20]. If the HE concept works in DRX cathodes, one would expect that increasing the number of TM species in them will improve Li transport properties by preventing the formation of a single dominant SRO type. Such SRO reduction should result in improved capacity and rate capability.

Here, to evaluate our HE DRX design strategy, three prototype compositions with an increasing number of TM species are investigated, as shown in Figure 1a. All three compositions include 30% Li excess (i.e., $Li_{1.3}$ per formula unit) to ensure good Li transport without severely compromising the TM redox capacity, and 15% oxygen substituted by fluorine to increase the TM redox reservoir [21,22]. The Mn^{3+}–Ti^{4+} combination[16] was used as baseline, with the $Li_{1.3}Mn^{3+}_{0.4}Ti_{0.3}O_{1.7}F_{0.3}$ composition referred to as TM2 hereafter. Mn^{2+}, Nb^{5+}, Co^{2+}, and Cr^{3+} were sequentially incorporated to form $Li_{1.3}Mn^{2+}_{0.2}Mn^{3+}_{0.2}Ti_{0.1}Nb_{0.2}O_{1.7}F_{0.3}$ and $Li_{1.3}Mn^{2+}_{0.1}Co^{2+}_{0.1}Mn^{3+}_{0.1}Cr^{3+}_{0.1}Ti_{0.1}Nb_{0.2}O_{1.7}F_{0.3}$, which contain four and six TM species and are therefore referred to as TM4 and TM6, respectively. We find indeed that while these compounds retain the same long-range order (LRO), the SRO becomes sequentially more suppressed as the number of TMs increases, leading to significant improvements in energy density and rate capability. This success motivated us to investigate the compatibility of different TM species to facilitate future experimental realizations of high-energy-density HE DRX cathodes. As further proof of the synthetic accessibility of HE DRX compounds, we successfully synthesized a phase-pure DRX composed of twelve TM species in similar concentrations.

Results

Structural characterization

All three compounds with different numbers of TM species were successfully synthesized using a traditional solid-state method. Scanning electron microscopy (SEM) analysis reveals that the particle size of the as-synthesized materials reaches approximately 5–10 μm (upper panel of Figure 1b, Figure S1) and can be reduced to 200–500 nm (lower panel of Figure 1b, Figure S1) by shaker milling with carbon during electrode fabrication. Synchrotron X-ray diffraction (XRD) patterns

(Figure 1c) and time-of-flight (TOF) neutron diffraction patterns (Figure S2) confirm the formation of single-phase DRX compounds with no observable impurity peaks. Elemental analysis confirms that the metal ratios in the as-synthesized materials are close to the target compositions, as shown in Table S1. Rietveld refinement yields lattice constants of 4.1918, 4.2286, and 4.2544 Å for TM2, TM4, and TM6, respectively. Scanning transmission electron microscope (STEM)/Energy-dispersive spectroscopy (EDS) was applied to investigate the distribution of the multiple elements in the materials. Figure 1d presents the STEM/EDS mapping of a representative particle of the as-synthesized TM6, showing that the different TMs and F are uniformly distributed within the particle. ^{19}F and ^{7}Li solid-state Nuclear Magnetic Resonance (ssNMR) measurements were further conducted to demonstrate the bulk F incorporation and to detect possible impurities (Figure S3, Supplementary Note 1).

The cation SRO in the three materials was evaluated using TEM electron diffraction, as shown in Figure 1e–1g. The round Bragg diffraction spots can be indexed to the *Fm-3m* space group and originate from the average rocksalt lattice. The square-like diffuse scattering patterns are attributed to SRO. [16,23,24] The intensity of the diffuse scattering, which qualitatively correlates with the strength of the SRO, was integrated within the dashed rectangular regions and compared across the three compounds. The results, displayed to the right of the electron diffraction patterns, clearly indicate that increasing the number of TM species from two to six suppresses the SRO in the DRX structures, as evidenced by the reduced intensity of the SRO pattern in the electron diffraction patterns. The experimental observation of the reduction in SRO from TM2 to TM6 is further corroborated computationally, as presented in Figure S6 and Supplementary Note 3.

Electrochemical performance

The electrochemical performance of the three materials was evaluated using galvanostatic cycling. When cycled between 1.5 and 4.7 V at a rate of 20 mA g^{-1}, TM2 delivers a capacity (specific energy) of 220 mAh g^{-1} (704 Wh kg^{-1}), as shown in Figure 2a. With more TM species in the DRX structure, TM4 delivers 269 mAh g^{-1} (849 Wh kg^{-1}) (Figure 2b), which further increases to 307 mAh g^{-1} (955 Wh kg^{-1}) for TM6 (Figure 2c). An extensive set of additional compositions containing subsets of the six TMs in the TM6 were synthesized and characterized (shown in Figure S5 and Supplementary Note 2), corroborating the overall trend that a larger number of TM species, rather than the incorporation of any specific TM, leads to a higher capacity. Galvanostatic intermittent titration (GITT) measurements (shown in Figure S4a) were also performed, indicating that the polarization is greatly reduced as the number of TM species in the DRX structure increases. The results support our design strategy of reducing SRO to improve Li transport, increase capacity, and reduce polarization.

The benefits of increasing the TM variety are further corroborated by rate performance tests on the three materials, as shown in Figure 2d–2f. For TM2, the discharge capacity decreases from 220 mAh g^{-1} when cycled at 20 mA g^{-1} to 58 mAh g^{-1} at 2000 mA g^{-1}, corresponding to a 74% capacity loss at the high rate. For a similar rate increase, the fraction of capacity loss is reduced to 58% for TM4 and to 45% for TM6. The rate capability of the TM6 compound is remarkable, with a discharge capacity of more than 170 mAh g^{-1} delivered at the very high cycling rate of 2,000 mA g^{-1}, corresponding to a 7 min (dis)charge process.

Redox mechanism

The redox behavior in the three materials was elucidated by combining hard X-ray absorption spectroscopy (hXAS) to capture the TM electronic states, and soft X-ray resonant inelastic X-ray

scattering (RIXS) for the oxygen state. The TM redox behavior in TM6 was studied using *in-situ* hXAS, with experimental details provided in the methods section. The X-ray near-edge structure (XANES) spectra of the pristine, top-of-charge, and end-of-discharge states at the Cr, Mn, and Co K-edge XAS are presented in Figure 3a–3c, respectively. Representative oxide references are also shown to facilitate the data interpretation. The oxidation states of Cr are estimated from the pre-edge intensity [25], and those of Mn and Co are estimated from the energy of the rising edge [26]. It can be estimated from Figure 3a that approximately 70% of Cr^{3+} is oxidized to Cr^{6+} at the top of charge, which contributes ~65 mAh g^{-1} capacity. As observed in Figure 3b, the Mn K-edge shifts to a higher energy and approaches that of MnO_2 (Mn^{4+}) when charged to 4.7 V. Full oxidation of Mn should contribute ~90 mAh g^{-1} capacity. The Co K-edge only shifts up close to that of the Co_3O_4 reference at the top-of-charge state which suggests the oxidation of Co^{2+} to approximately $Co^{8/3+}$, equivalent to ~20 mAh g^{-1} capacity contribution. Upon discharge, all three metal K-edges shift back to their initial energy positions, indicating good reversibility of the metal redox. The Co^{2+}/Co^{3+} and Cr^{3+}/Cr^{6+} redox processes are both only partially utilized, along with the full utilization of the Mn^{2+}/Mn^{4+} redox, leading to approximately 175 mAh g^{-1} of the overall capacity being contributed by the TM redox during the first cycle. Results and analysis of the TM redox behavior at other states of charge are presented in Figures S7-S8 and Supplementary Note 4.

A TM redox capacity that is much smaller than the observed reversible capacity, suggests the participation of oxygen redox, which is a phenomenon that often arises in Li-rich cathode materials. [27,28] We therefore performed high-efficiency mapping of O-*K* RIXS to detect any changes of the oxygen electronic states. Previous studies have established that O-*K* RIXS mapping can circumvent the limitation of conventional O-*K* XAS and therefore serves as the tool-of-choice for detecting lattice oxygen redox[29]. Particularly, a feature at the excitation energy of ~531 eV and

emission energy of ~524 eV is found to be a fingerprint of oxidized oxygen in a range of battery electrodes[29,30]. Indeed, comparing the O-*K* RIXS maps from pristine and top-of-charge of TM6 (Figure 3d,3e) clearly reveals the characteristic oxidized oxygen feature at 4.7 V (red arrow in Figure 3e), indicating some oxygen oxidation upon charge. RIXS cuts at the characteristic 531 eV excitation energy at three states of charge (pristine, charged and discharged) during the first cycle are provided in Figure 3f. The strong feature of oxidized oxygen (dashed line) appears at 4.7 V and disappears when fully discharged, indicating reversible oxygen oxidation and reduction processes.

The redox mechanisms in TM2 and TM4 were studied by similar methods (Figure S10–S12, Supplementary Note 5), confirming that Mn is mostly oxidized to Mn^{4+} in both materials, contributing approximately 140 mAh g^{-1} (TM2) and 180 mAh g^{-1} (TM4) to the overall capacity. The remainder of the capacity in both materials is provided by oxygen redox, as suggested by additional O-*K* RIXS results (Figure S11). These observations indicate that there is no significant difference in the redox behavior of the three materials, further confirming that an increased theoretical TM redox capacity is not the main reason for the improved capacities when increasing the number of TM species from TM2 to TM4/TM6.

Discussion

Given that DRX materials have generally suffered from low rate capability [15,16] , the high rates that can be achieved with the TM6 compound are remarkable. The rate capability and capacity in DRX materials seems to be largely connected to the percolation of 0-TM channels, the connection of tetrahedral units on which no TM is present[15,16]. While for fully random cation systems, percolation theory predicts 0-TM percolation to be prevalent for the 0.3Li excess used in our

compounds, SRO (i.e. deviations from the random state) has been shown to reduce percolation in a very significant way [16,19,31]. In particular, SRO of the γ–$LiFeO_2$–type which exhibits a preference for tetrahedral units with 2 Li and 2 TM are electrostatically favored but have a destructive effect on 0-TM percolation.[14] The prevalence of this SRO type is remarkable given γ–$LiFeO_2$–type LRO is not that common.[32] This may be because in long-ranged ordered structures, elastic energy contributions, originating from the size difference of the ions, are very important and often select the α–$NaFeO_2$–type layered structure.[33] Without such long-range interactions, γ–$LiFeO_2$–type SRO becomes prevalent in the disordered state, leading to degradation of Li transport.[14] For this reason, the ability to reduce or eliminate cation SRO is an important design insight. Our strategy to minimize SRO by the use of many different TM species, all in similar concentration, was inspired by the recent observations of nearly-random cation distribution in several metal and oxide HE compounds[11,12]. As our work shows, this strategy also works in DRX oxides: by increasing the number of TM species, the intensity of SRO is significantly reduced, as evidenced by the TEM electron diffraction results shown in Figure 1e–g. Consistent with our understanding of percolation theory, this then also improves capacity and rate performance (Figure 2).

To understand how broad the opportunity space is of possible HE-DRX compounds, we use *ab-initio* methods to evaluate which metals and valence states may coexist in a DRX compound. We approached this by estimating the mixing temperature of potential DRX compounds from the calculated energy difference between a structure with pseudo-random cations and the competing phases in the convex hull, as described in the Methods section. The mixing temperature is considered a qualitative measure of the synthetic accessibility, with a lower mixing temperature indicating better synthesizability, as it requires less thermal energy to mix the metal ions. Twenty-three cations were considered, i.e., Mn^{2+}, Fe^{2+}, Co^{2+}, Ni^{2+}, Mg^{2+}, Zn^{2+}, Cr^{3+}, V^{3+}, Mn^{3+}, Fe^{3+}, Co^{3+},

Ni^{3+}, Ga^{3+}, Al^{3+}, Ti^{4+}, Zr^{4+}, Mn^{4+}, V^{4+}, Sn^{4+}, Mo^{4+}, Nb^{5+}, V^{5+}, and Sb^{5+}. All possible combinations of these elements that fall into our five prototype compositions ($Li_{1.3}$ and $F_{0.3}$ per f.u., see Methods section) were considered, yielding 7965 distinct compounds. Compounds containing 2 or 3 TM species are defined as low-entropy DRX (LE DRX), while those with at least 4 TM species are defined as high-entropy DRX (HE DRX). The resulting probability distribution of the mixing temperature is plotted in Figure 4a. In addition, the boxplots in the top panel show the most likely range of mixing temperature for both LE and HE DRX materials. Given the approximations (DFT, quasi-random structure for the random state, and approximate entropy model), this temperature should not be taken as quantitative, but we expect qualitative differences between compound groups to be well represented. The approximate mixing temperatures of HE DRX compounds are generally more than 500K lower than those of LE DRXs. In other words, when synthesized at the same temperature, HE DRXs will be structurally more random.

Our data set also enables us to identify chemistries that are particularly well suited to create accessible low-SRO DRX compounds. The periodic table in Figure 4b shows (with color scale) the median mixing temperature of the systems that contain the given element. In the LE DRX, Ti and Mo enhance disorder, consistent with their presence in many DRX compositions[15,20]. For HE DRX, the chemical variation of the mixing temperature is considerably less, consistent with the idea that it is the extra entropy from the high number of elements that lowers the mixing temperature, rather than chemical specificity. This can be clearly observed for elements such as Mg^{2+}, Cr^{3+}, and Sb^{5+}, which are subject to forming secondary phases in LE DRXs but are more likely to be incorporated in HE DRXs.

In Figure 4c we compare the redox compatibility and chemical compatibility of TM ion pairs. Cation pairs that are not redox-compatible, i.e. they were found to transfer charge between them

when present together, are greyed out. For example, when Mn^{3+} and V^{3+} coexist in a DRX compound, charge transfer occurs, oxidizing V^{3+} to V^{5+} while reducing Mn^{3+} to Mn^{2+}, which is consistent with a previous finding that V^{4+}/V^{5+} oxidation occurs prior to Mn^{2+}/Mn^{3+} oxidation upon charge in a Mn^{2+}–V^{4+}-based DRX cathode [34]. The full map of charge-transfer and potential redox reactions between various TM pairs is presented in Figure S18. The chemical compatibility is quantified by the median mixing temperature of the compounds that contain both elements. The compatibility of different TM pairs is shown on a normalized scale between 0 (highly compatible) and 1 (not compatible) in Figure 4c. The scale is derived from the mixing temperatures as $T - T_{min})/(T_{max} - T_{min})$, in which T_{max} and T_{min} are the maximum and minimum mixing temperatures among all the TM pairs. Almost all the redox-active species, except Cr^{3+}, demonstrate good chemical compatibility when redox compatibility is satisfied. Species such as Mg^{2+}, Zn^{2+}, Ga^{3+}, Al^{3+}, Sn^{4+} are less compatible with the other TMs and their concentrations should be kept low. Following these guidelines, a HE DRX compound containing twelve TM species each at similar concentration was designed (Figure 4d) and successfully prepared using a traditional solid-state method. The XRD pattern (Figure 4d middle panel) confirms the phase purity without observable impurities, and the TEM–EDS mapping (Figure 4d lower panel) also indicates a homogeneous distribution of all the elements. We note that although it shows reasonable capacity (Figure S14), the TM12 compound is not optimized for electrochemical performance but as a demonstration that DRX materials containing such a high number of TM components can be synthesized.

While mixing a large number of TM ions can serve as a general strategy to suppress SRO and improve Li transport in DRXs, enough TM redox capacity needs to be maintained to achieve good electrochemical performance. There can be a trade-off between “high-entropy” and “high energy-

density" because incorporating more TM species would dilute the concentration of each TM, especially the redox-active TMs. Thus, the mixing of various redox-active TMs is a good strategy to frustrate SRO without diluting the TM redox capacity. The incorporation of double-redox centers, such as Mn^{2+} (Mn^{2+} / Mn^{4+}), V^{3+} (V^{3+} / V^{5+}), and Mo^{4+} (Mo^{4+} / Mo^{6+}) is especially beneficial because they provide high electron capacities and are compatible with each other in their low oxidation states. Cr^{3+} offers a three-electron redox (Cr^{3+} / Cr^{6+}) with a high voltage, however it tends to form competing layered phases, which limits the solubility of Cr^{3+} in a DRX compound (Supplementary Note 6). Note that because of their overlap with oxygen oxidation, Fe^{2+}, Co^{2+} and Ni^{2+} are regarded as one-electron redox centers in DRXs as demonstrated before[35,36], although their oxidation to a +4 state may be achieved in other structures[26,37]. High-valent d^0 TM species, such as Ti^{4+}, Nb^{5+}, demonstrate low mixing temperatures and are well compatible with most of the redox-active TMs, and thus can be used as charge compensators to further increase the TM redox capacity.

In addition, several practical issues are worth noting regarding the potential engineering and commercialization of HE DRX cathodes. DRX cathodes often exhibit larger voltage hysteresis (Supplementary Figure S4b) than conventional layered ones, such as Li-stoichiometric NMC (Ni, Co, Mn) oxides, the precise origin of which is so far unclear. Furthermore, while the bulk DRX lattice remains intact and robust upon cycling (Figure S15), which may further be enhanced by the entropy-stabilization effect[12] in HE DRXs, cathode-electrolyte interfacial reactions (Figure S16), might still occur and result in capacity degradation upon cycling. For example, TM6 shows slightly worse capacity retention (around 76% retained after 20 cycles) than that of TM2 (84% after 20 cycles) and TM4 (80% after 20 cycles). This can presumably be attributed to the larger degree of

cathode-electrolyte interfacial side-reactions in TM6, as indicated by a higher amount of CO_2 evolution observed in the DEMS tests (Figure S12, S13).

Outlook for HE DRX cathodes

The concept of HE compounds has become increasingly important in materials science, because of its wide applicability to various fields and its ability to enlarge the design space for functional materials. The outstanding chemical flexibility of the DRX compounds makes them an ideal platform to exercise this opportunity and create cathode materials that combine high energy density and high rate capability. As demonstrated in this work, the cathode compound composed of six different TM species achieves capacity >300 mAh g^{-1} with energy density >950 Wh kg^{-1} at 20 mA g^{-1}, which is approximately 40% larger than the capacity of the low-entropy TM2 compound. In addition, the incorporation of a large number of TM species reduces the extent of SRO in the DRX lattice and dramatically improves Li transport. TM6 exhibits excellent rate capability, retaining a discharge capacity of >170 mAh g^{-1} when cycled at a very high rate of 2 A g^{-1}. This allows a complete (dis)charge within 7 min, with a gravimetric capacity delivered comparable to that of $LiCoO_2$.

We believe that the combination of chemical flexibility of DRX materials, and the ability to improve Li-transport by creating more random configurations with a high number of metal components, as demonstrated in this paper, creates a potentially vast space of interesting new cathode compounds. To navigate this space, our thermodynamic analyses of the compatibility between various TM pairs reveal two important guidelines (i.e. redox compatibility and chemical compatibility) when designing HE DRX cathodes. From the perspective of compositional design, a Li-excess level of 1.2-1.3 per f.u. is typically suggested, which is expected to provide a

reasonable amount of percolating Li without too much limiting the TM redox capacity. Fluorination can be applied to further increase the TM redox reservoir, which is beneficial for cycle life. When mixing many species to suppress the unfavorable SRO, prioritizing the use of redox-active TMs is preferred for a large TM capacity. TM ions capable of multi-electron redox and with good chemical compatibility, such as Mn^{2+}, and V^{3+}, are highly preferred, while a small amount of the less-soluble Cr^{3+} is also beneficial for its high-voltage three-electron redox process. Fe^{2+} (to provide Fe^{2+} / Fe^{3+} redox capacity) may also be a good redox center, with a low mixing temperature and high natural abundance. For non-redox-active species, high-valence metal ions, such as Ti^{4+} and Nb^{5+}, can be used as charge compensators to enable a larger TM redox reservoir. Additional factors, such as the concentration of each TM component within a fixed HE chemical space, or even the synthesis condition (Figure S20, Supplementary Note 7) are also expected to affect the configurational entropy, the degree of SRO, and thus the electrochemical performance. Further exploration of advanced HE DRX cathodes is likely to lead to even more improved cathode materials. We would also call for investigations on the capacity fading mechanism in DRX cathodes, such as the effect of electrolyte breakdown at the high voltage cutoff typically used for DRX materials. New electrolyte strategies or surface protection are expected to enhance the cycle life of the HE DRX cathodes. In addition, optimization of the rate capability, as presented in this work and other [38] may allow for larger particle sizes to be used which would reduce surface reactivity.

Methods

Synthesis

All the DRX oxyfluoride compounds were synthesized using a traditional solid-state method. Li_2CO_3 (Alfa Aesar, ACS, 99% min), MnO (Stream Chemicals Inc., 99%), $CoCO_3$ (Alfa Aesar, 99.5%), Mn_2O_3 (Alfa Aesar, 99.9%), Cr_2O_3 (Sigma-Aldrich, 98%), TiO_2 (Alfa Aesar, 99.9%), Nb_2O_5 (Sigma-Aldrich, 99.99%), and LiF (Alfa Aesar, 99.99%) were used as precursors. For TM12, additional precursors of Fe_2O_3 (Aldrich, nano-powder), Ga_2O_3 (Alfa Aesar, 99.999%), $Zr(OH)_4$ (Aldrich, 97%), Sb_2O_5 (Alfa Aesar, 99.998%), Ta_2O_5 (Aldrich, 99.99%), and MgF_2 (Sigma-Aldrich, 99.9%) were used. All the precursors were stoichiometrically mixed in ethanol (except that around 10% more Li_2CO_3 and 5% more $CoCO_3$ were added to compensate for possible loss during synthesis) with a Retsch PM 400 planetary ball mill at a rate of 180 rpm for 12 h. The precursors were then dried in an oven at 70°C overnight and pelletized. The precursor pellets were pre-heated at 600°C for 3 h followed by sintering at 1000°C under an argon atmosphere, except for TM2, MCN, and MCT, which were sintered at 1050°C. The duration of sintering was 6 h. The pellets were then fast cooled in an argon atmosphere, transferred to a glovebox, and ground into powders.

Electrochemistry

All the cathode films were composed of the active materials, Super C65 (Timcal), and polytetrafluoroethylene (PTFE, DuPont, Teflon 8A) at a weight ratio of 70:20:10. To make the cathode films, 280 mg of the as-synthesized active materials and 80 mg of Super C65 were mixed and shaker-milled for 90 min in an argon atmosphere using a SPEX 800M mixer/mill, and PTFE was later added and manually mixed with the shaker-milled mixture for 40 min. The components were then rolled into thin films inside a glovebox. Commercial 1 M $LiPF_6$ in ethylene carbonate (EC) and dimethyl carbonate (DMC) solution (1:1 volume ratio) was used as the electrolyte. A glass microfiber filter (Whatman) was used as the separator. FMC Li metal foil was used as the

anode. Coin cells were assembled inside the glovebox and tested on an Arbin battery test instrument at room temperature. The loading density of the films was approximately 3–4 mg cm^{-2} based on the active materials. For the rate-capability tests, a smaller loading density of approximately 2.5 mg cm^{-2} based on the active materials was used. The specific capacities were calculated based on the weight of active materials (70%) in the cathode films. For the GITT measurements, each step in the voltage profiles corresponds to a galvanostatic charge/discharge of 10 mAh g^{-1} at a rate of 20 mA g^{-1} followed by a 6-h relaxation step.

Characterization

Synchrotron XRD patterns of the as-synthesized compounds were obtained at Beamline 28-ID-2 at Brookhaven National Lab. Lab XRD patterns were obtained using a Rigaku Miniflex 600 or a Bruker D8 ADVANCE diffractometer (Cu source) in the 2θ range of 15°–85°. Rietveld refinement was performed using PANalytical X'pert HighScore Plus software. Elemental analysis was performed using direct current plasma emission spectroscopy (PerkinElmer Optima 5300 DV Optical Emission Spectrometer) for lithium, titanium, chromium, manganese, cobalt, and niobium. The fluorine content was measured using a Cole-Parmer PB-2750414 fluoride ion-selective electrode. SEM images were collected using a Zeiss Gemini Ultra-55 analytical field-emission SEM at the Molecular Foundry at Lawrence Berkeley National Lab (LBNL). Scanning transmission electron microscopy (STEM)/EDS/electron diffraction (ED) measurements were performed on a JEM-2010F and Titan X microscopes at the Molecular Foundry at LBNL. To compare the intensity of EDs, the same acquisition time was used and all the particles examined are similar in size. Neutron powder diffraction analysis was performed using the Nanoscale Ordered Materials Diffractometer (NOMAD) at the Spallation Neutron Source at Oak Ridge

National Laboratory. The samples for the neutron diffraction experiment were prepared using ^{7}Li-enriched precursors (^{7}LiF and $^{7}Li_2CO_3$). The refinement was performed using TOPAS software.

Solid-state nuclear magnetic resonance (NMR) spectroscopy

Solid-state nuclear magnetic resonance (ssNMR) data were collected on the TM2, TM4, and TM6 pristine powders using a Bruker Advance 300 MHz (7.05 T) wide-bore NMR spectrometer with Larmor frequencies of 282.40 and 116.64 MHz at room temperature. The data were obtained at 60-kHz magic-angle spinning (MAS) using a 1.3-mm double-resonance HX probe. ^{19}F and ^{7}Li NMR data were referenced against lithium fluoride (LiF, $\delta(^{19}F) = -204$ ppm and $\delta(^{7}Li) = -1$ ppm). Lineshape analysis was performed using the Bruker Topspin software and SOLA lineshape simulation package.

The resonant frequency range of ^{19}F nuclei in TM2, TM4, and TM6 was larger than the excitation bandwidth of the RF pulse used in the NMR experiment. To obtain the full spectrum, eleven spin echo spectra were collected for TM2 and nine spin echo spectra were collected for TM4 and TM6. These spectra were obtained using frequency steps of 140 ppm (739.5 kHz) from −759 to 361 ppm, where the step size was slightly less than the excitation bandwidth of the RF pulse. Individual sub-spectra were processed using a zero-order phase correction and then added to give an overall sum spectrum in absorption mode that required no further phase correction. This method — termed 'frequency stepping' [39,40], 'spin echo mapping' [41], or 'VOCS' [42] (variable offset cumulative spectrum) — uniformly excites the broad ^{19}F signals by providing a large excitation bandwidth. Individual ^{19}F spin echo spectra were collected using a 90° RF pulse of 5.2 μs and a 180° RF pulse of 10.4 μs at 100 W, with a recycle delay of 30 ms. For reference, a spin echo spectrum was collected on LiF using similar RF pulses but with a recycle delay of 30 s. A ^{19}F spectrum obtained

on the empty probe using acquisition parameters similar to those used for the ^{19}F spectra collected on the DRX samples showed no significant background signal.

^{7}Li spin echo spectra of all the samples were obtained using a 90° radiofrequency (RF) pulse of 0.7 μs and a 180° RF pulse of 1.4 μs at 100 W. A recycle delay of 30 s was used for LiF, and a recycle delay of 0.5 s was used for all the DRX samples. Additional spin echo spectra were acquired with a recycle delay of 3 s for TM4 and TM6 to capture the entire ^{7}Li diamagnetic signal for quantification purposes; this was unnecessary for TM2, as ^{7}Li spin lattice relaxation was much faster for this compound.

Ex-situ and *operando* hard X-ray absorption spectroscopy (XAS)

X-ray absorption spectroscopy (XAS) spectra were acquired in transmission mode at beamline 20-BM-B at the Advanced Photon Source. The incident beam energy was selected using a Si (111) monochromator. The energy calibration was performed by simultaneously measuring the spectra of an appropriate metal foil. Harmonic rejection was accomplished using a Rh-coated mirror. All the *ex-situ* samples were electrode films composed of active materials, Super C65, and PTFE in a weight ratio of 70:20:10, and the loading density (based on the active materials) was determined using Hephaestus software. They were assembled as coin cells, charged to the designated capacities, and then disassembled and washed with DMC in a glovebox (except for the pristine materials). Additional spectra of reference standards were also measured to facilitate interpretation. *Operando* hard XAS spectra of TM6 at the Cr, Mn, and Co K-edges were measured using a modified coin-cell setup within the voltage window of 1.5–4.7 V at a cycling rate of 16 mA g^{-1}. The cell was held at the top of charge for 30 min before discharging. The loading density (based on the active material) was approximately 10 mg cm^{-3}. The raw data were processed (normalization and energy calibration) using Athena software.[43]

Resonant inelastic X-ray scattering (RIXS)

O-K RIXS maps were obtained at beamline 8.0.1 at the iRIXS endstation at the Advanced Light Source. The cathode samples were mounted on a 1-inch copper sample holder and transferred from an argon glovebox into the ultrahigh vacuum main chamber using a sealed sample transfer kit. The beam slit size was set to 40/40, and the samples were continuously moved within a small region relative to the focused beam position to minimize photo damage. The photon energy was calibrated using the first peak of the standard TiO_2 as 531 eV. The emission spectra at each excitation energy were collected for 90 s. The RIXS map was generated from the emission spectra at different excitation energies using an Igor code written by the Yang group. The emission energy was calibrated based on the elastic peak line on the RIXS map. Key samples such as the pristine, fully charged, and fully discharged were measured multiple times, each with fresh sample preparation.

Differential electrochemical mass spectrometer (DEMS) measurement

The custom-built differential electrochemical mass spectrometry (DEMS) instrument, cell geometry, and instrument operation are described in previous publications[44-46]. The electrochemical cells used with the DEMS device were prepared in a glove box using a modified Swagelok design, and the cathode film was composed of the active materials, carbon black, and PTFE in a weight ratio of 70:20:10, with a loading density of ~10 mg cm^{-2} (based on the active materials). The electrolyte, separators, and anodes used were identical to those used for the coin-cell tests in this study. The assembled cells were charged at 20 mA g^{-1} (except for the multi-cycle test, which used a rate of C/10) under a static head of positive argon pressure (approximately 1.2 bar) at room temperature after being appropriately attached to the DEMS instrument. The accumulated gas in the cell was purged by 500 μL of pulsed argon gas every 10 minutes. The swept-out gas was subsequently sent into Mass-Spectrometry chamber for analysis. Calibration of

the mass spectrometry at various partial pressure of O_2, CO_2, or H_2 in argon was conducted for quantification. CO evolution was estimated by the method described in the previous publication [47]. Mass-spectrometer signals of POF_3 fragments (m/z 104 and m/z 85) were used to monitor POF_3 release.

Density functional theory calculations

First-principles density functional theory (DFT) calculations were performed to obtain an accurate description of the structural energies and oxidation states of the different cathode materials. All the calculations were performed using the projector-augmented wave (PAW) method[48] as implemented in the Vienna Ab initio Simulation Package (VASP)[49]. A rotationally averaged Hubbard U correction[50,51] was used to correct the self-interaction error in oxides containing Co, Cr, Fe, Mn, Mo, Ni, and V. The U parameters were obtained from a previously reported calibration to oxide formation energies[51]. For all the calculations, a reciprocal space discretization of 25 k-points per $Å^{-1}$ was applied, and the convergence criteria were set as 10^{-6} eV for electronic loops and 0.02 eV $Å^{-1}$ for ionic loops.

Special quasi-random structure and mixing temperature calculation

Special quasi-random structures (SQSs) are periodic structures whose atomic distributions are selected such that the cluster correlations approach the expected value in a random atomic arrangement as closely as possible for a given structure size[52]. Given this feature, SQSs are an appropriate choice to investigate the properties of rocksalt materials with full disorder. In the alloy community, for example, SQSs have been successfully used to evaluate mixing enthalpies[53] and to model the electronic structure of random alloys[54]. Our previous studies on DRXs using SQS structures also indicate that these structures can be effective tools for quantifying the phase stability[55], electronic structure[20], and voltage curves[56,57]. To model the random cation distribution

of the fully disordered rocksalt materials, we generated SQS structures for all three prototype compositions, i.e., $Li_{1.3}(M_a)^{3+}_{0.4}(M_b)^{4+}_{0.3}O_{1.7}F_{0.3}$, $Li_{1.3}(M_a)^{2+}_{0.2}(M_b)^{3+}_{0.2}(M_c)^{4+}_{0.1}(M_c)^{5+}_{0.2}O_{1.7}F_{0.3}$, and $Li_{1.3}(M_a)^{2+}_{0.1}(M_b)^{2+}_{0.1}(M_c)^{3+}_{0.1}(M_d)^{3+}_{0.1}(M_e)^{4+}_{0.1}(M_f)^{5+}_{0.2}O_{1.7}F_{0.3}$, as well as two additional compositions containing three TMs and five TMs, respectively, i.e., $Li_{1.3}(M_a)^{2+}_{0.3}(M_b)^{3+}_{0.1}(M_c)^{5+}_{0.3}O_{1.7}F_{0.3}$ and $Li_{1.3}(M_a)^{2+}_{0.1}(M_b)^{2+}_{0.1}(M_c)^{3+}_{0.2}(M_d)^{4+}_{0.1}(M_e)^{5+}_{0.2}O_{1.7}F_{0.3}$. With the energetics calculated from DFT, the mixing temperature of DRX materials was estimated using the equation

$$T_{mixing} = \frac{E_{hull}}{k_b(0.65ln0.65 + 0.15ln0.15 + 0.85ln0.85 + \sum_M x_M lnx_M)}.$$

E_{hull} is the energy above the convex hull per cation in the phase diagram constructed with all phases in the relevant chemical space available in an internal database containing phases from the ICSD as well as some compounds generated using data-mined substitution rules.[58] The variable x_M refers to the atomic fraction of metal per cation site. The DRXs with only two or three TMs are grouped into LE DRXs, whereas those containing more than three TMs are classified as HE DRXs. The mixing temperature of a specific DRX composition is calculated as its energy above the convex hull divided by the maximum configurational entropy it gains upon disordering. A complete list of all competing phases generated by our phase diagram analysis is provided in Supplementary Table 2.

Cluster expansion, Monte Carlo simulation, SRO and percolation analysis

A cluster expansion model has been constructed to describe the energetics of the complete configurational space of Li^{+}-Mn^{2+}-Co^{2+}-Mn^{3+}-Cr^{3+}-Ti^{4+}-Nb^{5+}-O^{2-}-F^{-}. In such a cluster expansion, the configurational energy dependence is captured by an expansion into different cluster functions, which can be formulated as [59,60]:

$$E = \sum_{i,sp1} J_i^{sp1} \sigma_i^{sp1} + \sum_{i,j,sp1,sp2} J_{ij}^{sp1sp2} \sigma_i^{sp1} \sigma_j^{sp2} + \sum_{i,j,k,sp1,sp2,sp3} J_{ijk}^{sp1sp2sp3} \sigma_i^{sp1} \sigma_j^{sp2} \sigma_k^{sp3} \ldots\ldots$$

Here, σ_i^{sp} corresponds to the occupancy of a certain site(s) with a certain species *sp* and *J* refers to the effective cluster interactions (ECIs).

In HE-DRX material, a cation site can be occupied by Li and six other types of metals while the anion sites can be occupied by either O^{2-} or F^-. For each system, pair interactions up to 7.1 Å, triplet interactions up to 4.0 Å, and quadruplet interactions up to 4.0 Å based on a rocksalt lattice with a cubic lattice parameter a = 3.0 Å were included in the cluster-expansion formulism. The ECIs were fitted to DFT energies of sampled structures using a L1-regularized least-squares regression approach[61], with the regularization parameters selected to minimize cross-validation error [17,19,34,61-63]. The DFT results of 6154 structures are applied to fit the cluster expansion, which end up with a cluster expansion model that has root-mean-squared error of 7.62 meV/atom.

With the constructed cluster expansion, we then perform Monte Carlo simulation at 1273K for three experimental compositions, i.e., TM2, TM4 and TM6. For each composition, percolation analysis [14,19] and Warren-Cowley SRO parameter [64] calculations are performed on 10000 MC structures.

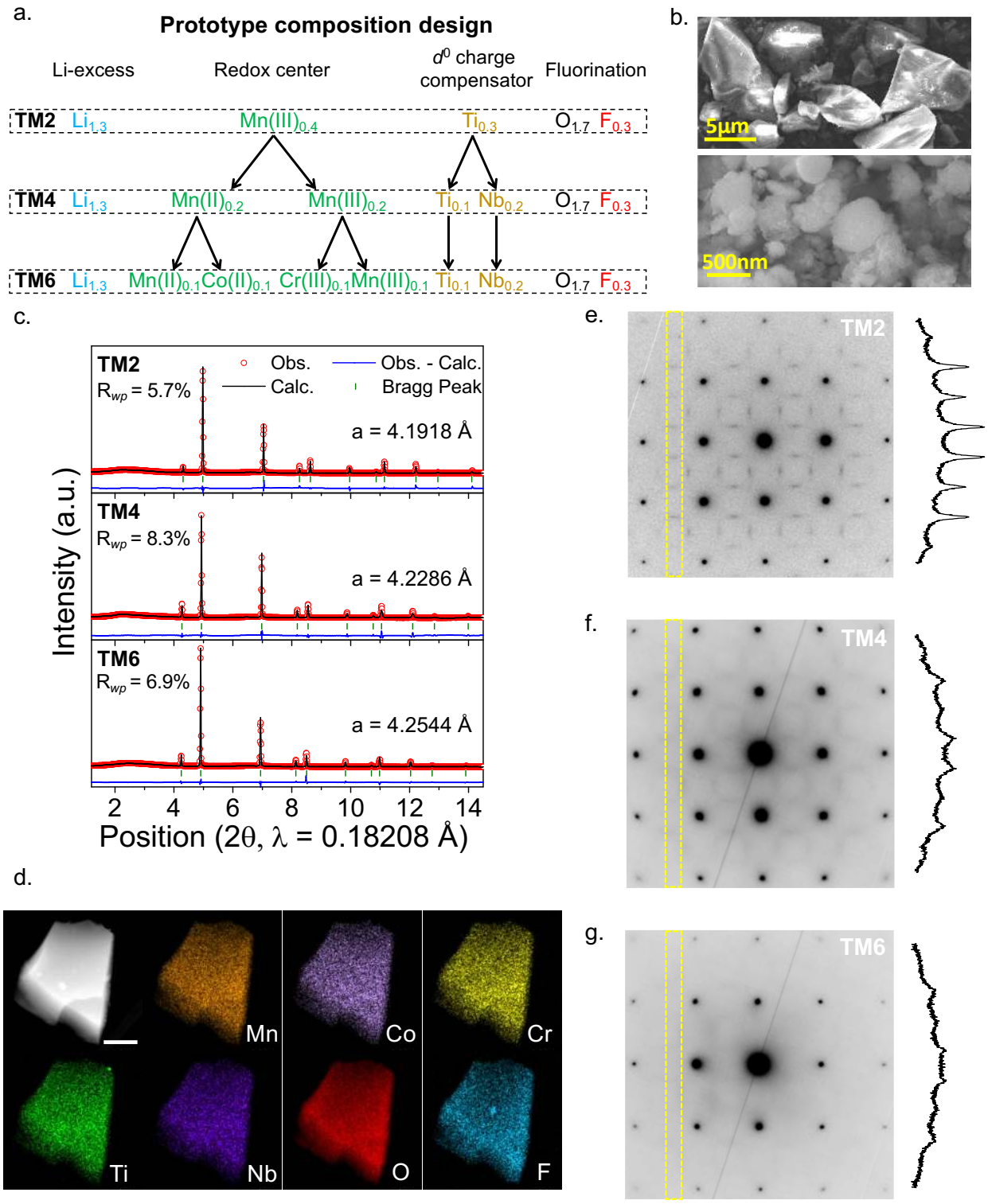

Figure 1 | Design and structural characterization of the as-synthesized materials. a. Prototype composition design of DRX cathodes with different numbers of TMs. **b.** SEM images of as-

synthesized (upper panel) TM6 and TM6 shaker-milled with carbon black (lower panel). **c.** Synchrotron XRD patterns and refined lattice constants of the as-synthesized materials at λ=0.18208 Å. **d.** TEM/EDS mapping of elemental distribution in a particle cluster of as-synthesized TM6 (Scale bar: 300nm). TEM ED patterns collected on as-synthesized **e.** TM2, **f.** TM4, and **g.** TM6 along the [100] zone axis. The round spots, which originate from the LRO in the materials, are indexed to the Fm-3m space group. The square-like diffuse scattering patterns are attributed to the SRO. Quantifications of the SRO pattern intensity by integrating the counts within the dashed rectangular regions are displayed next to the ED patterns.

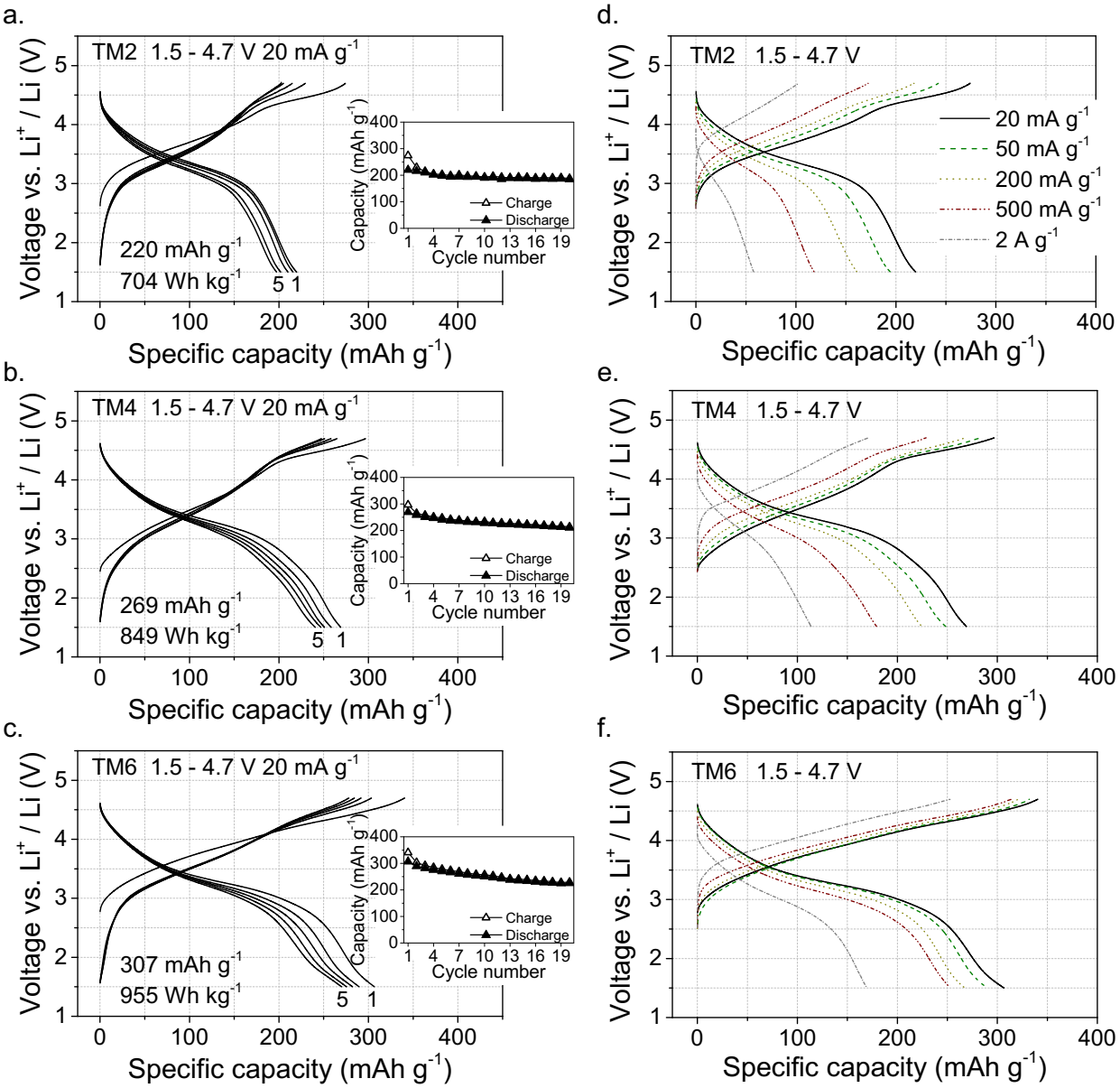

Figure 2 | Electrochemical performance of the three compounds. Voltage profiles and capacity retention of **a.** TM2, **b.** TM4, and **c.** TM6 within the voltage window of 1.5–4.7 V at 20 mA g^{-1} and room temperature. Rate capability of **d.** TM2, **e.** TM4, and **f.** TM6: the first-cycle voltage profiles of all three compounds when cycled between 1.5 and 4.7 V at 20, 50, 200, 500, and 2,000 mA g^{-1}.

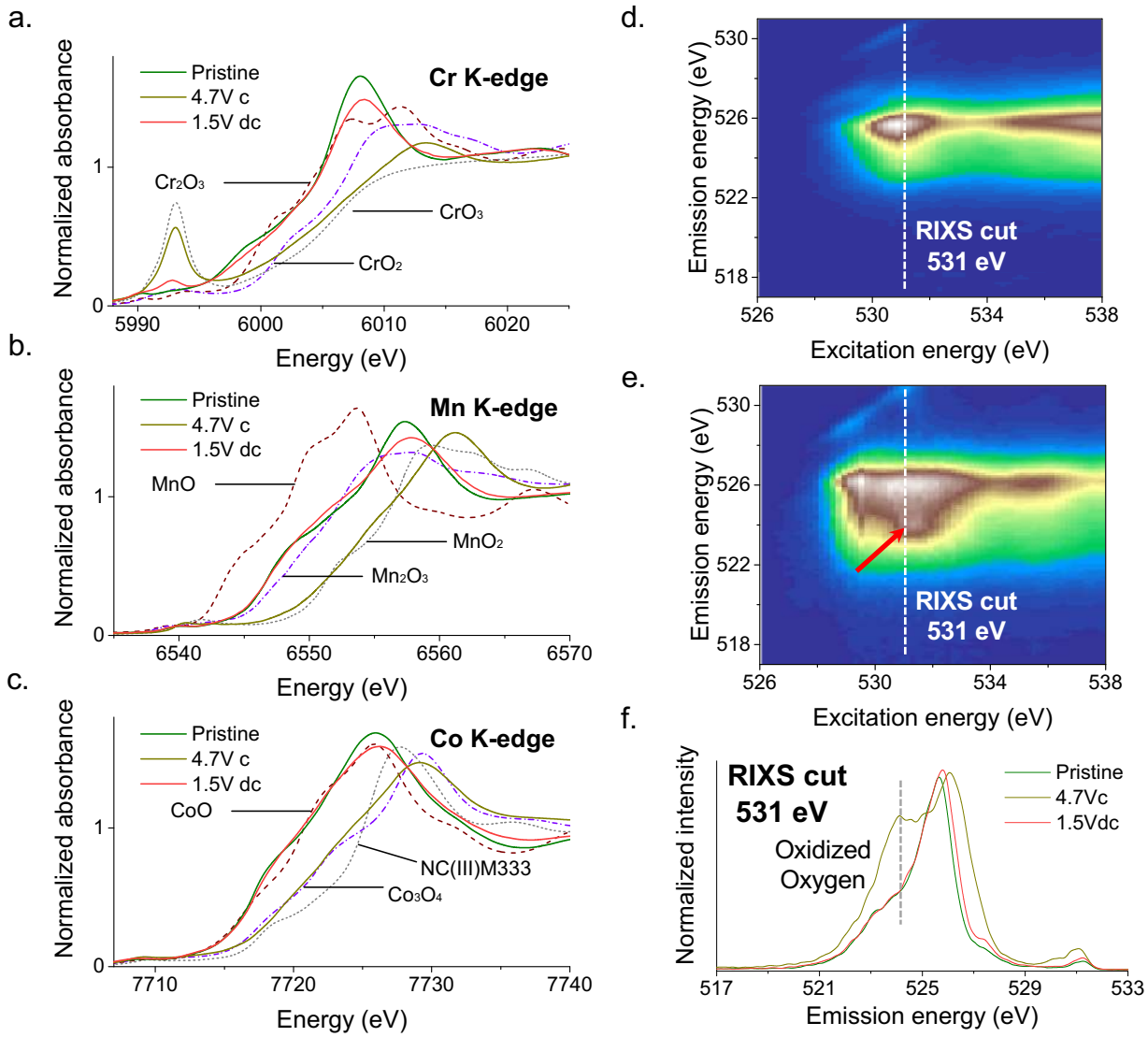

Figure 3 | Redox mechanism of TM6. XANES spectra in pristine, top-of-charge (4.7 V c), and end-of-discharge (1.5 V dc) state from first cycle at **a.** Cr K-edge, **b.** Mn K-edge, and **c.** Co K-edge acquired from *operando* XAS measurement. *O-K* RIXS map of TM6 in **d.** pristine and **e.** top-of-charge state (4.7 V). The red arrow marks the oxidized oxygen feature. **f.** *O-K* RIXS spectra collected at an excitation energy of 531 eV (marked by the dashed lines in **3d.** and **3e.**) in pristine, top-of-charge (4.7 V c), and end-of-discharge (1.5 V dc) state from first cycle. The dashed line marks the oxidized oxygen feature.

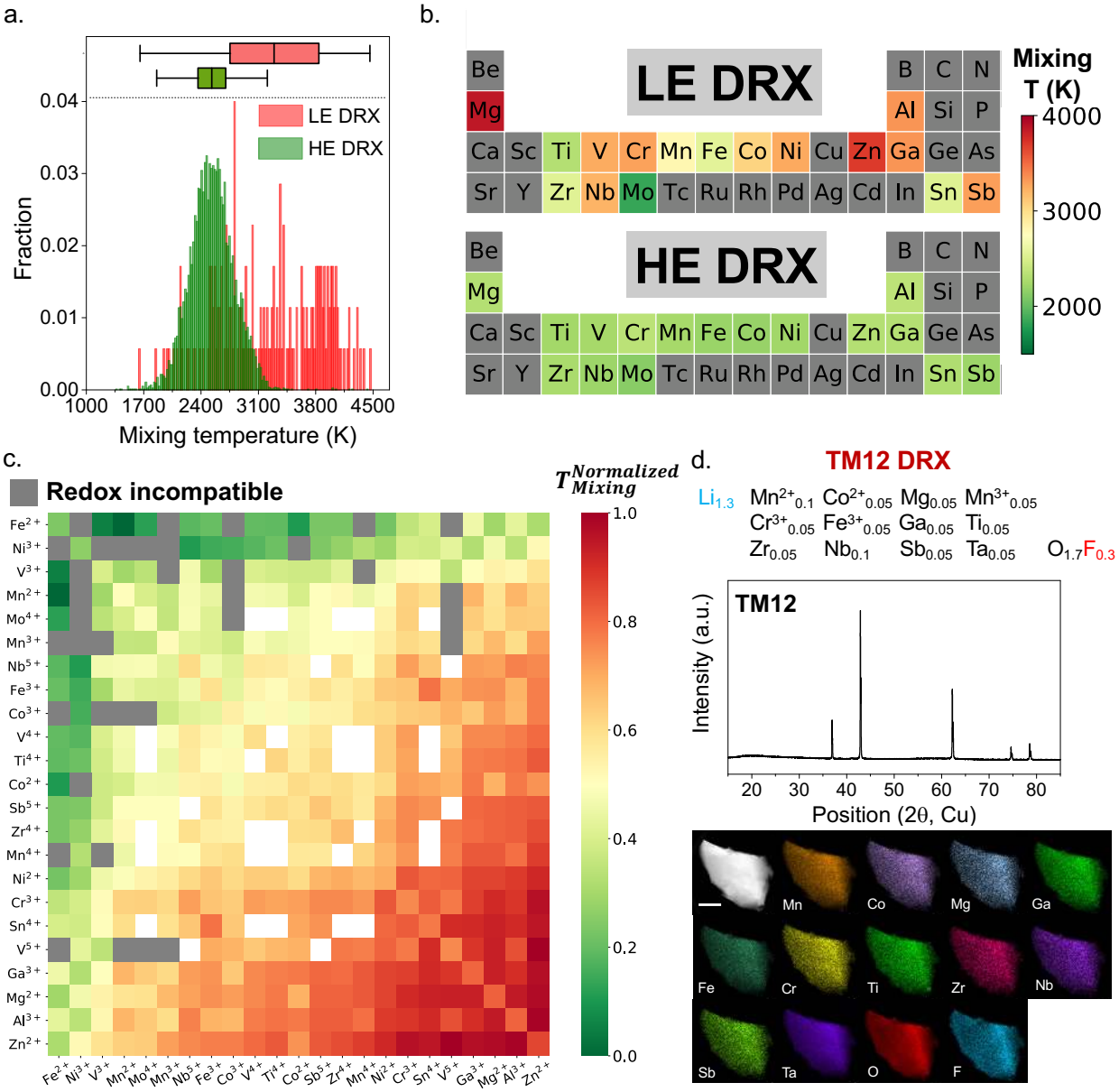

Figure 4 | Compatibility of metals in HE DRX cathodes. a. Probability distribution of mixing temperature for LE and HE DRX cathodes. The box chart plot on the top shows the median and interquartile range of mixing temperatures for LE and HE DRXs. **b.** Periodic-table-type heat map of mixing temperatures of different elements in LE and HE DRXs. The elements colored grey were not included in the calculations. **c.** Normalized compatibility of different TM species in DRX compounds. The color bar from green to red indicates increasing incompatibility. See text for details on the normalized quantity plotted. Grey fields are redox incompatible couples. White square are TM couples that were not included in our compositions. **d.** Demonstration of a HE DRX

containing 12 TM species (TM12). The XRD pattern confirms the phase purity and the TEM–EDS mapping shows the uniform distribution of different elements. (Scale bar: 400nm)

Data availability

Source data for the figures are provided with the paper. All relevant data within the article are available from the corresponding author upon reasonable request.

Reference

1 Cantor, B., Chang, I. T. H., Knight, P. & Vincent, A. J. B. Microstructural development in equiatomic multicomponent alloys. *Materials Science and Engineering: A* **375-377**, 213-218, doi:https://doi.org/10.1016/j.msea.2003.10.257 (2004).

2 Yeh, J. W. *et al.* Nanostructured high-entropy alloys with multiple principal elements: novel alloy design concepts and outcomes. *Advanced Engineering Materials* **6**, 299-303 (2004).

3 Zhang, R.-Z. & Reece, M. J. Review of high entropy ceramics: design, synthesis, structure and properties. *Journal of Materials Chemistry A* **7**, 22148-22162 (2019).

4 Oses, C., Toher, C. & Curtarolo, S. High-entropy ceramics. *Nature Reviews Materials*, doi:10.1038/s41578-019-0170-8 (2020).

5 Zhang, R.-Z., Gucci, F., Zhu, H., Chen, K. & Reece, M. J. Data-Driven Design of Ecofriendly Thermoelectric High-Entropy Sulfides. *Inorganic chemistry* **57**, 13027-13033 (2018).

6 Batchelor, T. A. A. *et al.* High-Entropy Alloys as a Discovery Platform for Electrocatalysis. *Joule* **3**, 834-845, doi:https://doi.org/10.1016/j.joule.2018.12.015 (2019).

7 Bérardan, D., Franger, S., Meena, A. & Dragoe, N. Room temperature lithium superionic conductivity in high entropy oxides. *Journal of Materials Chemistry A* **4**, 9536-9541 (2016).

8 Wang, Q. *et al.* Multi-anionic and-cationic compounds: New high entropy materials for advanced Li-ion batteries. *Energy & Environmental Science* (2019).

9 Sarkar, A. *et al.* High entropy oxides for reversible energy storage. *Nature Communications* **9**, 3400, doi:10.1038/s41467-018-05774-5 (2018).

10 Zhao, C., Ding, F., Lu, Y., Chen, L. & Hu, Y.-S. High-entropy chemistry stabilizing layered O3-type structure in Na-ion cathode. *Angewandte Chemie International Edition* (2019).

11 Harrington, T. J. *et al.* Phase stability and mechanical properties of novel high entropy transition metal carbides. *Acta Materialia* **166**, 271-280 (2019).

12 Rost, C. M. *et al.* Entropy-stabilized oxides. *Nature communications* **6**, 8485 (2015).

13 Lee, J. *et al.* Unlocking the potential of cation-disordered oxides for rechargeable lithium batteries. *Science* **343**, 519-522 (2014).
14 Urban, A., Lee, J. & Ceder, G. The Configurational Space of Rocksalt-Type Oxides for High-Capacity Lithium Battery Electrodes. *Advanced Energy Materials* **4**, 1400478 (2014).
15 Clément, R. J., Lun, Z. & Ceder, G. Cation-disordered rocksalt transition metal oxides and oxyfluorides for high energy lithium-ion cathodes. *Energy & Environmental Science* **13**, 345-373, doi:10.1039/C9EE02803J (2020).
16 Ji, H. *et al.* Hidden structural and chemical order controls lithium transport in cation-disordered oxides for rechargeable batteries. *Nature Communications* **10**, 592, doi:10.1038/s41467-019-08490-w (2019).
17 Lun, Z. *et al.* Design Principles for High-Capacity Mn-Based Cation-Disordered Rocksalt Cathodes. *Chem*, doi:https://doi.org/10.1016/j.chempr.2019.10.001 (2019).
18 Clément, R. J., Kitchaev, D., Lee, J. & Gerbrand, C. Short-Range Order and Unusual Modes of Nickel Redox in a Fluorine-Substituted Disordered Rocksalt Oxide Lithium-Ion Cathode. *Chemistry of Materials* **30**, 6945-6956, doi:10.1021/acs.chemmater.8b03794 (2018).
19 Ouyang, B. *et al.* Effect of Fluorination on Lithium Transport and Short-Range Order in Disordered-Rocksalt-Type Lithium-Ion Battery Cathodes. *Advanced Energy Materials* **10**, 1903240, doi:10.1002/aenm.201903240 (2020).
20 Urban, A., Abdellahi, A., Dacek, S., Artrith, N. & Ceder, G. Electronic-Structure Origin of Cation Disorder in Transition-Metal Oxides. *Physical review letters* **119**, 176402 (2017).
21 Chen, R. *et al.* Disordered Lithium-Rich Oxyfluoride as a Stable Host for Enhanced Li+ Intercalation Storage. *Advanced Energy Materials* **5**, 1401814-n/a, doi:10.1002/aenm.201401814 (2015).
22 Lee, J. *et al.* Reversible Mn2+/Mn4+ double redox in lithium-excess cathode materials. *Nature* **556**, 185-190, doi:10.1038/s41586-018-0015-4 (2018).
23 De Ridder, R., van Tendeloo, G. & Amelinckx, S. A cluster model for the transition from the short-range order to the long-range order state in f.c.c. based binary systems and its study by means of electron diffraction. *Acta Crystallographica Section A* **32**, 216-224, doi:doi:10.1107/S0567739476000508 (1976).
24 Hata, S., Matsumura, S., Kuwano, N. & Oki, K. Short range order and its transformation to long range order in Ni4Mo. *Acta Materialia* **46**, 881-892, doi:https://doi.org/10.1016/S1359-6454(97)00314-5 (1998).
25 Balasubramanian, M., McBreen, J., Davidson, I., Whitfield, P. & Kargina, I. In situ X-ray absorption study of a layered manganese-chromium oxide-based cathode material. *Journal of the electrochemical Society* **149**, A176-A184 (2002).
26 Yoon, W.-S. *et al.* Investigation of the charge compensation mechanism on the electrochemically Li-Ion deintercalated Li1-x Co1/3Ni1/3Mn1/3O2 electrode system by combination of soft and hard X-ray absorption spectroscopy. *Journal of the American Chemical Society* **127**, 17479-17487 (2005).
27 Luo, K. *et al.* Charge-compensation in 3d-transition-metal-oxide intercalation cathodes through the generation of localized electron holes on oxygen. *Nature Chemistry* **8**, 684, doi:10.1038/nchem.2471 (2016).
28 Seo, D.-H. *et al.* The structural and chemical origin of the oxygen redox activity in layered and cation-disordered Li-excess cathode materials. *Nature chemistry* **8**, 692 (2016).

29 Yang, W. & Devereaux, T. P. Anionic and cationic redox and interfaces in batteries: Advances from soft X-ray absorption spectroscopy to resonant inelastic scattering. *Journal of Power Sources* **389**, 188-197 (2018).
30 Dai, K. *et al.* High Reversibility of Lattice Oxygen Redox Quantified by Direct Bulk Probes of Both Anionic and Cationic Redox Reactions. *Joule* **3**, 518-541, doi:10.1016/j.joule.2018.11.014 (2019).
31 Jones, M. A. *et al.* Short-range ordering in a battery electrode, the 'cation-disordered'rocksalt Li 1.25 Nb 0.25 Mn 0.5 O 2. *Chemical Communications* **55**, 9027-9030 (2019).
32 Hewston, T. A. & Chamberland, B. L. A Survey of first-row ternary oxides LiMO2 (M = Sc-Cu). *Journal of Physics and Chemistry of Solids* **48**, 97-108, (1987).
33 Wu, E. J., Tepesch, P. D. & Ceder, G. Size and charge effects on the structural stability of LiMO2 (M= transition metal) compounds. *Philosophical Magazine B* **77**, 1039-1047 (1998).
34 Kitchaev, D. A. *et al.* Design principles for high transition metal capacity in disordered rocksalt Li-ion cathodes. *Energy & Environmental Science* **11**, 2159-2171, (2018).
35 Lee, J. *et al.* A new class of high capacity cation-disordered oxides for rechargeable lithium batteries: Li–Ni–Ti–Mo oxides. *Energy & Environmental Science* **8**, 3255-3265 (2015).
36 Yabuuchi, N. *et al.* Origin of stabilization and destabilization in solid-state redox reaction of oxide ions for lithium-ion batteries. *Nature communications* **7**, 13814 (2016).
37 Yabuuchi, N. *et al.* P2-type Nax[Fe1/2Mn1/2]O2 made from earth-abundant elements for rechargeable Na batteries. *Nature Materials* **11**, 512-517, doi:10.1038/nmat3309 (2012).
38 Ji, H. *et al.* Ultrahigh power and energy density in partially ordered lithium-ion cathode materials. *Nature Energy* **5**, 213-221, doi:10.1038/s41560-020-0573-1 (2020).
39 O'Dell, L. A., Rossini, A. J. & Schurko, R. W. Acquisition of ultra-wideline NMR spectra from quadrupolar nuclei by frequency stepped WURST–QCPMG. *Chemical physics letters* **468**, 330-335 (2009).
40 Pell, A. J., Clément, R. J., Grey, C. P., Emsley, L. & Pintacuda, G. Frequency-stepped acquisition in nuclear magnetic resonance spectroscopy under magic angle spinning. *The Journal of Chemical Physics* **138**, 114201 (2013).
41 Sananes, M., Tuel, A., Hutchings, G. & Volta, J. Characterization of different precursors and activated vanadium phosphate catalysts by 31P NMR spin echo mapping. *Journal of Catalysis* **148**, 395-398 (1994).
42 Massiot, D. *et al.* 71Ga and 69Ga nuclear magnetic resonance study of β-Ga2O3: resolution of four-and six-fold coordinated Ga sites in static conditions. *Solid State Nuclear Magnetic Resonance* **4**, 241-248 (1995).
43 Ravel, B. & Newville, M. ATHENA, ARTEMIS, HEPHAESTUS: data analysis for X-ray absorption spectroscopy using IFEFFIT. *Journal of Synchrotron Radiation* **12**, 537-541, doi:doi:10.1107/S0909049505012719 (2005).
44 McCloskey, B. D., Bethune, D., Shelby, R., Girishkumar, G. & Luntz, A. Solvents' critical role in nonaqueous lithium–oxygen battery electrochemistry. *The Journal of Physical Chemistry Letters* **2**, 1161-1166 (2011).
45 McCloskey, B. D. *et al.* On the efficacy of electrocatalysis in nonaqueous Li–O2 batteries. *Journal of the American Chemical Society* **133**, 18038-18041 (2011).
46 McCloskey, B. D. *et al.* Twin problems of interfacial carbonate formation in nonaqueous Li–O2 batteries. *The journal of physical chemistry letters* **3**, 997-1001 (2012).

47 Renfrew, S. E. & McCloskey, B. D. Residual Lithium Carbonate Predominantly Accounts for First Cycle CO2 and CO Outgassing of Li-Stoichiometric and Li-Rich Layered Transition-Metal Oxides. *Journal of the American Chemical Society* **139**, 17853-17860, doi:10.1021/jacs.7b08461 (2017).
48 Kresse, G. & Joubert, D. From ultrasoft pseudopotentials to the projector augmented-wave method. *Physical Review B* **59**, 1758-1775, doi:10.1103/PhysRevB.59.1758 (1999).
49 Kresse, G. & Furthmüller, J. Efficiency of ab-initio total energy calculations for metals and semiconductors using a plane-wave basis set. *Computational Materials Science* **6**, 15-50, doi:https://doi.org/10.1016/0927-0256(96)00008-0 (1996).
50 Dudarev, S. L., Botton, G. A., Savrasov, S. Y., Humphreys, C. J. & Sutton, A. P. Electron-energy-loss spectra and the structural stability of nickel oxide: An LSDA+U study. *Physical Review B* **57**, 1505-1509, doi:10.1103/PhysRevB.57.1505 (1998).
51 Wang, L., Maxisch, T. & Ceder, G. Oxidation energies of transition metal oxides within the GGA+U framework. *Physical Review B* **73**, 195107, doi:10.1103/PhysRevB.73.195107 (2006).
52 Zunger, A., Wei, S. H., Ferreira, L. G. & Bernard, J. E. Special quasirandom structures. *Physical Review Letters* **65**, 353-356, doi:10.1103/PhysRevLett.65.353 (1990).
53 Shin, D., van de Walle, A., Wang, Y. & Liu, Z.-K. First-principles study of ternary fcc solution phases from special quasirandom structures. *Physical Review B* **76**, 144204, doi:10.1103/PhysRevB.76.144204 (2007).
54 Wei, S. H., Ferreira, L. G., Bernard, J. E. & Zunger, A. Electronic properties of random alloys: Special quasirandom structures. *Physical Review B* **42**, 9622-9649, doi:10.1103/PhysRevB.42.9622 (1990).
55 Urban, A., Matts, I., Abdellahi, A. & Ceder, G. Computational Design and Preparation of Cation-Disordered Oxides for High-Energy-Density Li-Ion Batteries. *Advanced Energy Materials* **6**, 1600488, doi:10.1002/aenm.201600488 (2016).
56 Abdellahi, A., Urban, A., Dacek, S. & Ceder, G. The Effect of Cation Disorder on the Average Li Intercalation Voltage of Transition-Metal Oxides. *Chemistry of Materials* **28**, 3659-3665, doi:10.1021/acs.chemmater.6b00205 (2016).
57 Abdellahi, A., Urban, A., Dacek, S. & Ceder, G. Understanding the effect of cation disorder on the voltage profile of lithium transition-metal oxides. *Chemistry of Materials* **28**, 5373-5383 (2016).
58 Hautier, G., Fischer, C., Ehrlacher, V., Jain, A. & Ceder, G. Data Mined Ionic Substitutions for the Discovery of New Compounds. *Inorganic Chemistry* **50**, 656-663, doi:10.1021/ic102031h (2011).
59 Sanchez, J. M., Ducastelle, F. & Gratias, D. Generalized cluster description of multicomponent systems. *Physica A: Statistical Mechanics and its Applications* **128**, 334-350, doi:https://doi.org/10.1016/0378-4371(84)90096-7 (1984).
60 Wolverton, C. & de Fontaine, D. Cluster expansions of alloy energetics in ternary intermetallics. *Physical Review B* **49**, 8627-8642, doi:10.1103/PhysRevB.49.8627 (1994).
61 Nelson, L. J., Hart, G. L. W., Zhou, F. & Ozoliņš, V. Compressive sensing as a paradigm for building physics models. *Physical Review B* **87**, 035125, doi:10.1103/PhysRevB.87.035125 (2013).
62 Richards, W. D., Dacek, S. T., Kitchaev, D. A. & Ceder, G. Fluorination of Lithium-Excess Transition Metal Oxide Cathode Materials. *Advanced Energy Materials* **8**, 1701533, doi:doi:10.1002/aenm.201701533 (2018).

63 Ji, H. *et al.* Computational Investigation and Experimental Realization of Disordered High-Capacity Li-Ion Cathodes Based on Ni Redox. *Chemistry of Materials* **31**, 2431-2442, doi:10.1021/acs.chemmater.8b05096 (2019).
64 Cowley, J. M. X-Ray Measurement of Order in Single Crystals of Cu3Au. *Journal of Applied Physics* **21**, 24-30, doi:10.1063/1.1699415 (1950).

Acknowledgements

This work was supported by the Umicore Specialty Oxides and Chemicals, the Assistant Secretary for Energy Efficiency and Renewable Energy, Vehicle Technologies Office, of the U.S. Department of Energy under Contract No. DEAC02-05CH11231, under the Advanced Battery Materials Research (BMR) Program. Work at the Molecular Foundry was supported by the Office of Science, Office of Basic Energy Sciences, of the U.S. Department of Energy under contract No. DE-AC02-05CH11231. The NMR experimental work reported here made use of the shared facilities of the UCSB MRSEC (NSF DMR 1720256), a member of the Material Research Facilities Network. This research used resources at the Spallation Neutron Source, a DOE Office of Science User Facility operated by the Oak Ridge National Laboratory. This research used resources from beamline 28-ID of the National Synchrotron Light Source II, a U.S. Department of Energy (DOE) Office of Science User Facility operated for the DOE Office of Science by Brookhaven National Laboratory under Contract No. DE-SC0012704. Work at the Advanced Light Source is supported by DOE Office of Science User Facility under contract no. DE-AC02-05CH11231. This research used resources of the Advanced Photon Source, an Office of Science User Facility operated for the U.S. Department of Energy (DOE) Office of Science by Argonne National Laboratory, and was supported by the U.S. DOE under Contract No. DE-AC02-06CH11357. The computational analysis was performed using computational resources sponsored by the Department of Energy's Office of Energy Efficiency and Renewable Energy and located at the National Renewable Energy Laboratory, computational resources provided by Extreme

Science and Engineering Discovery Environment (XSEDE), which was supported by National Science Foundation grant number ACI1053575, as well as the National Energy Research Scientific Computing Center (NERSC), a DOE Office of Science User Facility supported by the Office of Science and the U.S. Department of Energy under Contract No. DE-AC02-05CH11231. The authors thank Dr. Jue Liu for the help of neutron diffraction measurement.

Author information

These authors contributed equally: Zhengyan Lun, Bin Ouyang.

Author contributions

Z.L. planned the project with H. J. and G.C.; Z.L. designed, synthesized, characterized (XRD) and electrochemically tested the proposed compounds with the help from Z.C., J.H., H. (Haegyeom) K. and H.J.; B.O. performed DFT, SQS calculations, cluster expansion, and Monto Carlo simulation and analyzed the data; D.H.K. acquired and analyzed TEM data; Y.H. acquired and analyzed the RIXS data with W.Y.; E.F. acquired and analyzed the NMR data with R.J.C.; T.-Y.H. acquired and analyzed DEMS data with input from B.D.M.; Z.L. acquired and analyzed the XAS data with the help from H. (Hyunchul) K., M.B., Z.C. and Y.S.; Y.T. performed SEM. The manuscript was written by Z.L. and was revised by B.O., R.J.C., H.J. and G.C. with the help of all other authors. All authors contributed to discussions.

Corresponding authors

Correspondence to Huiwen Ji, Gerbrand Ceder.

Competing interests

The authors declare no competing interests.

Electronic Supplementary Information

Cation-disordered rocksalt-type high-entropy cathodes for Li-ion batteries

Zhengyan Lun [†ab], Bin Ouyang [†ab], Deok-Hwang Kwon [ab], Yang Ha [c], Emily E. Foley [d], Tzu-Yang Huang [eg], Zijian Cai [ab], Hyunchul Kim [b], Mahalingam Balasubramanian [f], Yingzhi Sun [ab], Jianping Huang [b], Yaosen Tian [ab], Haegyeom Kim [b], Bryan D. McCloskey [eg], Wanli Yang [c], Raphaële J. Clément [d], Huiwen Ji [g*], Gerbrand Ceder [ab*]

[a] Department of Materials Science and Engineering, UC Berkeley, Berkeley, CA 94720, USA

[b] Materials Sciences Division, LBNL, Berkeley, CA 94720, USA

[c] Advanced Light Source, Lawrence Berkeley National Laboratory, Berkeley, CA 94720, USA

[d] Materials Department, University of California, Santa Barbara, CA 93106, USA

[e] Department of Chemical and Biomolecular Engineering, UC Berkeley, Berkeley, CA 94720, USA

[f] X-ray Science Division, Advanced Photon Source, Argonne National Laboratory, Argonne, IL 60439, USA

[g] Energy Storage and Distributed Resources Division, LBNL, Berkeley, CA 94720, USA

[†] These authors contributed equally.

[*] email: huiwenji@lbl.gov, gceder@berkeley.edu

This file includes

Supplementary Figures 1-20

Supplementary Notes 1-7

Supplementary Tables 1-2

Supplementary References

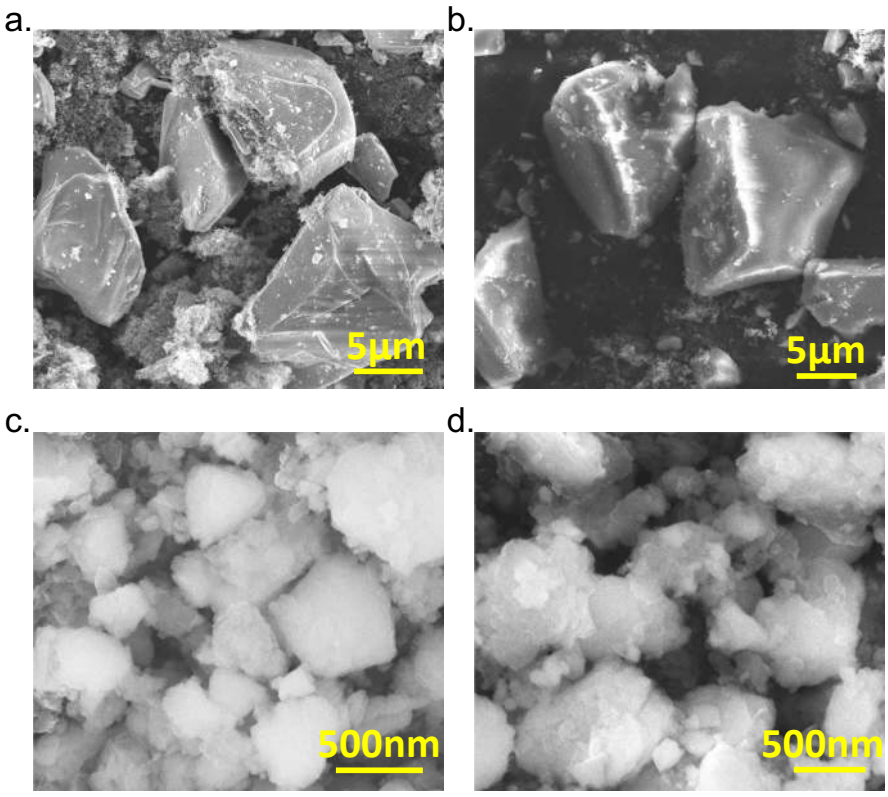

Figure S1 | SEM images of as-synthesized a. TM2 and **b.** TM4 **and shaker-milled c.** TM2 and **d.** TM4 **with carbon black**.

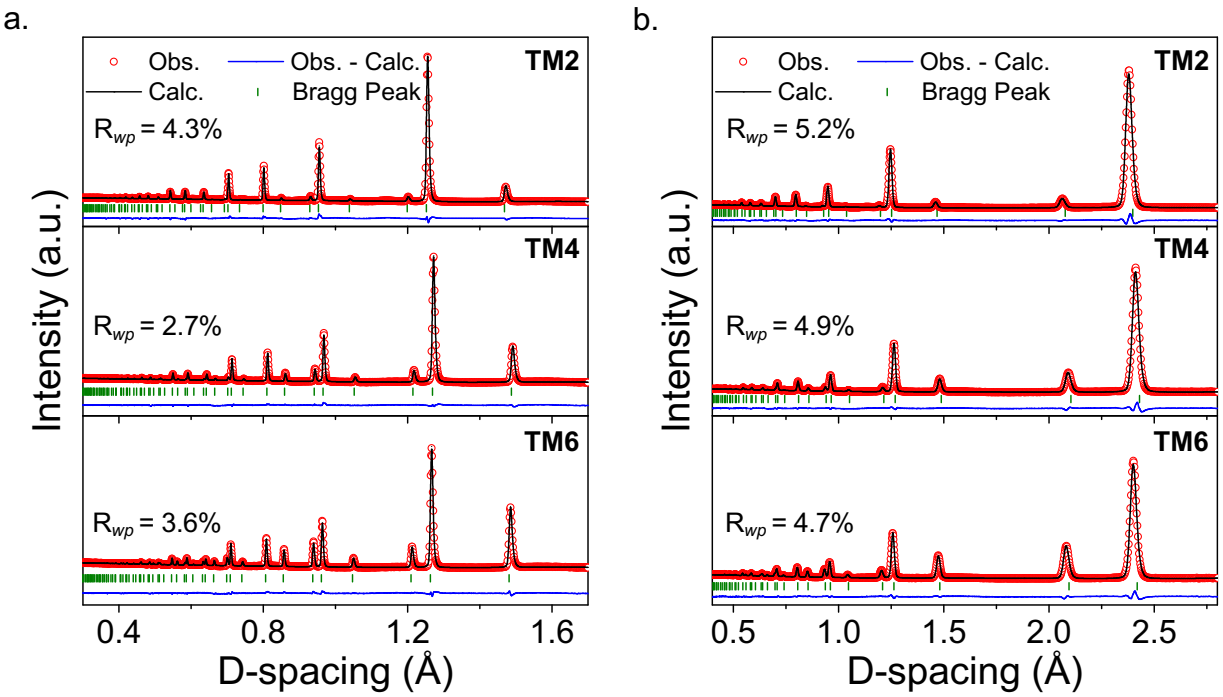

Figure S2 | Neutron diffraction patterns of as-synthesized materials. a. Bank 2 and **b.** Bank 3 neutron diffraction patterns of the as-synthesized TM2, TM4, and TM6 compounds.

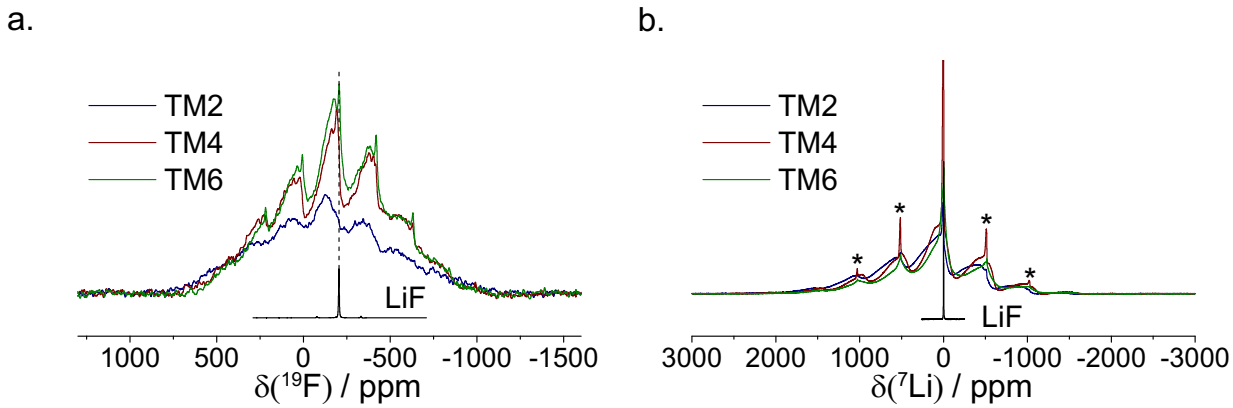

Figure S3 | ssNMR spectra obtained on the as-synthesized materials. a. ^{19}F ssNMR spectra obtained by summing over multiple spin echo sub-spectra acquired at different excitation frequencies to ensure homogeneous excitation of the broad lineshape. The spectra were scaled according to the amount of sample in the rotor and number of scans. For comparison, a ^{19}F spin echo spectrum collected on LiF powder is overlaid. **b.** ^{7}Li spin echo NMR spectra of the as-synthesized materials. For comparison, the ^{7}Li spin echo spectrum collected on LiF powder is overlaid. Spinning sidebands of the sharp, diamagnetic ^{7}Li signals (e.g., LiF, Li_2O, Li_2CO_3) are indicated with asterisks.

Supplementary Note 1: NMR spectra of as-synthesized DRXs

^{19}F NMR measurements were conducted to confirm the bulk incorporation of F into the DRX lattice rather than the formation of a separate LiF impurity phase, as shown in Figure S3a. The ^{19}F NMR spectra collected on the as-synthesized DRX materials differ significantly from the sharp spectrum obtained on the LiF reference. Generally speaking, strong paramagnetic interactions between unpaired *d* electrons on the TM ions (Mn^{2+}, Co^{2+}, Mn^{3+}, and Cr^{3+} in this case) and F nuclei lead to a shift of the ^{19}F resonant frequency away from that of the diamagnetic LiF at −204 ppm and significant spectral broadening. Hence, the broad ^{19}F spectra obtained on the as-synthesized DRX cathodes indicate bulk incorporation of F into the paramagnetic cathodes, as well as a distribution of resonant frequencies due to the formation of a range of local F environments in the disordered lattice. As discussed in previous work [1,2], when F ions are directly bonded to TM ions with unpaired *d* electrons, very strong paramagnetic interactions are generated, which result in signals that are too broad and/or decay too quickly to be observed. As a result, quantitative information on the distribution of the different F coordination environments

(paramagnetic vs. diamagnetic) cannot be obtained from the integration of the ^{19}F spectra. We also note that these spectra were acquired using a short recycle delay of 30 ms to maximize the signal-to-noise ratio, but which may not allow the ^{19}F NMR signal from diamagnetic sites in the sample to fully return to equilibrium between successive scans and may lead to a reduced apparent ^{19}F NMR signal from these environments. However, our previous ^{19}F ssNMR work on related DRX cathodes indicates that most of the diamagnetic ^{19}F signal is observed under such experimental conditions. Hence, the presence of a very low intensity diamagnetic signal in the spectra collected on TM2, TM4 and TM6 samples suggests that the majority of F ions are incorporated in the DRX phase.

The ^{7}Li spin echo NMR spectra collected on the three as-synthesized compounds and the LiF powder are presented in Figure S3b. Integration of the sharp signal at approximately 0 ppm in each of the spectra indicates that the fraction of Li present in diamagnetic environments (*e.g.*, in LiF, Li_2O, or Li_2CO_3 impurity phases) is less than 10%, 19%, and 11% (+/− 5%) in TM2, TM4, and TM6, respectively. This integration was performed on quantitative ^{7}Li spectra collected using optimized recycle delays of 0.5 s for TM2 and 3 s for TM4/TM6. We note that the intensity of the diamagnetic ^{7}Li signal gives the upper limits for the amount of impurity phases present in the samples because this signal could also be due to the formation of diamagnetic Li-rich (TM-poor) domains within the disordered oxide matrix [3]. Hence, both impurity particles and structurally-integrated diamagnetic domains arising from local segregation of cations in our compounds can, in theory, give rise to diamagnetic ^{7}Li environments. The absence of additional signals in our XRD and neutron scattering patterns suggests that the amount of impurities in the as-synthesized materials, if any, is small.

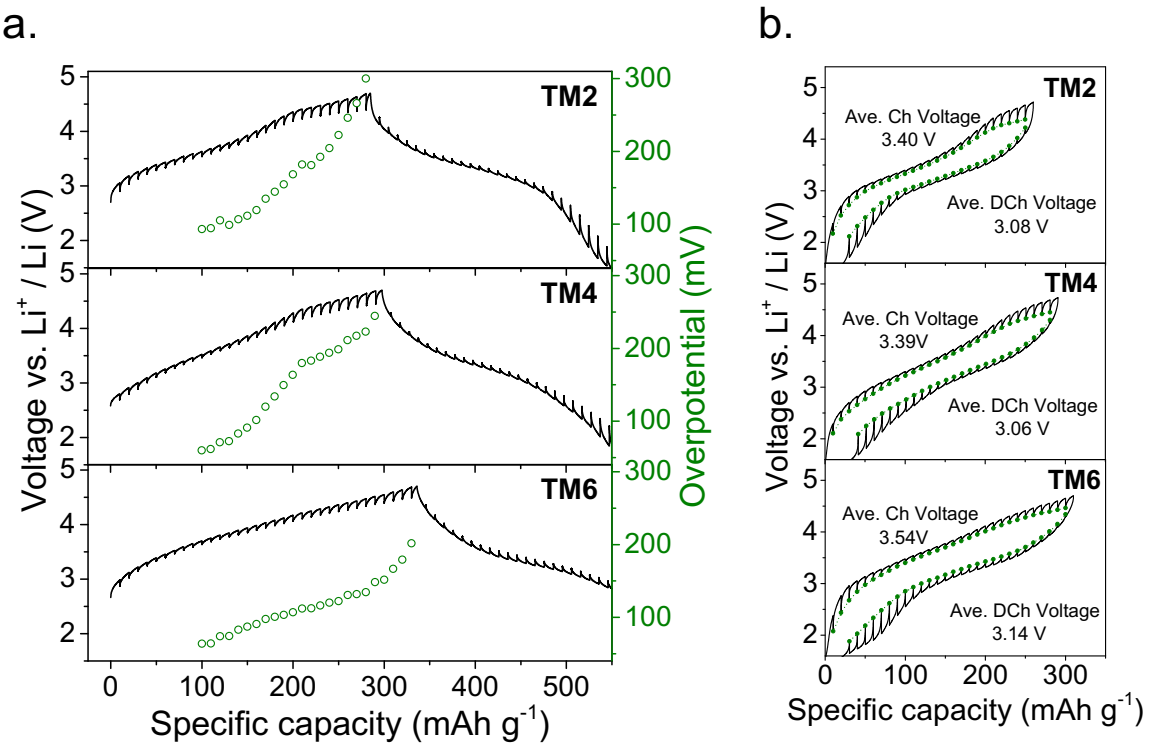

Figure S4 | Voltage profiles of TM2, TM4, and TM6 from GITT tests. Each step in the GITT voltage profiles corresponds to a galvanostatic charge/discharge of 10 mAh g^{-1} at a rate of 20 mA g^{-1} followed by a 6-h relaxation step. **a.** First-cycle voltage profiles of TM2, TM4 and TM6. The overpotentials at each step between 100 mAh g^{-1} charged states and the top-of-charge states are calculated and plotted as green dots in the figures. **b.** Second-cycle voltage profiles of TM2, TM4, and TM6 by GITT tests. The green dots mark the quasi-equilibrium voltage at each step. The average voltages after relaxation are calculated and noted in the figure. TM2 and TM4 show similar voltage hysteresis of 0.32V and 0.33V, respectively, while TM6 presents a slightly larger voltage hysteresis of 0.40V. We attribute the slightly larger voltage hysteresis in TM6 to the non-symmetric Cr^{3+}/Cr^{6+} oxidation and reduction processes, as discussed in Supplementary Note 4. This phenomenon, induced by Cr^{6+} migration, was also observed in many other Cr-containing cathodes. [4,5]

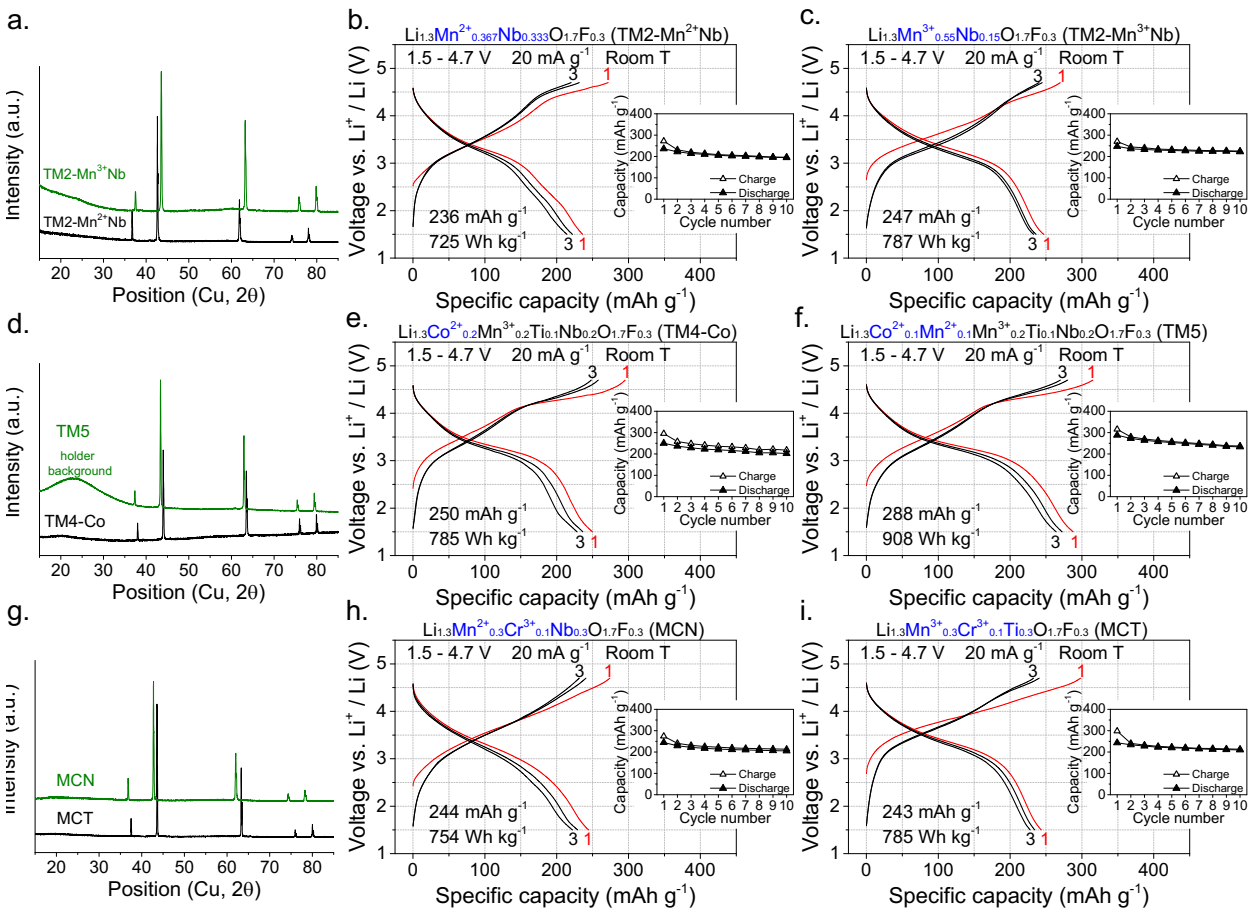

Figure S5 | Evaluations on the entropic effect. XRD patterns of **a.** TM2-Mn^{2+}Nb, TM2-Mn^{3+}Nb; **d.** TM4-Co, TM5; and **g.** MCN, MCT. Voltage profiles and capacity retention of **b.** TM2-Mn^{2+}Nb, **c.** TM2-Mn^{3+}Nb, **e.** TM4-Co, **f.** TM5, **h.** MCN and **i.** MCT within the voltage window of 1.5–4.7 V at 20 mA g^{-1} and room temperature.

Supplementary Note 2: Evaluation of the entropic effect on the capacity improvement from TM2 to TM4 and TM6

To further prove that the superior performance of TM6 is due to an entropic effect rather than a specific TM specie, we synthesized and characterized as many "low-entropy" compounds with the same elements as possible. What we have tried to do is to separate the effect of the different transition metals as much as possible by evaluating them in compounds with less components (so that they do not have the benefit of the high entropy).

First, we compare the performance of the TM4 ($Li_{1.3}Mn^{2+}_{0.2}Mn^{3+}_{0.2}Ti_{0.1}Nb_{0.2}O_{1.7}F_{0.3}$) in the manuscript with that of binary DRXs containing subgroups of the four TMs. We synthesized two new binaries, $Li_{1.3}Mn^{2+}_{0.367}Nb_{0.333}O_{1.7}F_{0.3}$ (TM2-Mn^{2+}Nb), $Li_{1.3}Mn^{3+}_{0.55}Nb_{0.15}O_{1.7}F_{0.3}$ (TM2-Mn^{3+}Nb), as shown in Figure S5 a-c. Along with the TM2 ($Li_{1.3}Mn^{3+}_{0.4}Ti_{0.3}O_{1.7}F_{0.3}$) reported in the draft, these four compounds share the same prototype composition "$Li_{1.3}TM_{0.7}O_{1.7}F_{0.3}$" and were synthesized using the same solid state method. We note that another binary compound $Li_{1.3}Mn^{2+}_{0.2}Ti_{0.5}O_{1.7}F_{0.3}$ cannot be obtained as pure phase as the product contains a second phase of LiF. Between them, the three binaries cover all the elements present in the quaternary. All of the binary compounds, including TM2 (220 mAh g^{-1}, Figure 2a), TM2-Mn^{2+}Nb (236 mAh g^{-1}, Figure S5b), and TM2-Mn^{3+}Nb (247 mAh g^{-1}, Figure S5c) exhibit a smaller capacity than that delivered by TM4 (269 mAh g^{-1}, Figure 2b). This confirms that mixing different TM species and hence a high configurational entropy brings out better electrochemical performance.

We then evaluate the roles of Co^{2+} and Cr^{3+}, the two species included in TM6 but not in TM4.

For Co^{2+}, we compare two new compositions, which are $Li_{1.3}Co^{2+}_{0.2}Mn^{3+}_{0.2}Ti_{0.1}Nb_{0.2}O_{1.7}F_{0.3}$ (TM4-Co) and $Li_{1.3}Co^{2+}_{0.1}Mn^{2+}_{0.1}Mn^{3+}_{0.2}Ti_{0.1}Nb_{0.2}O_{1.7}F_{0.3}$ (TM5) as shown in Figure S5d-f, with TM4 from the main text ($Li_{1.3}Mn^{2+}_{0.2}Mn^{3+}_{0.2}Ti_{0.1}Nb_{0.2}O_{1.7}F_{0.3}$). The higher-entropic TM5 has superior capacity (288 mAh g^{-1}, Figure S5f), as compared to the two "end members", TM4 (269 mAh g^{-1}, Figure 2b) and TM4-Co (250 mAh g^{-1}, Figure S5e), indicating that Co^{2+} on its own does not account for the improved capacity.

For Cr^{3+}, we evaluate two new Cr-containing ternary compounds (Figure S5 g-i). The Cr^{3+} concentration (0.1 per f.u.) in these two ternaries is the same as that in the TM6 compound. We did not pick binary compounds as comparison because the low solubility of Cr^{3+} in DRXs prevents us from getting phase-pure Cr-based binary DRX compounds using the same synthesis method by

which our other compounds are made (as discussed in Supplementary Note 6). When comparing $Li_{1.3}Mn^{2+}_{0.3}Cr^{3+}_{0.1}Nb_{0.3}O_{1.7}F_{0.3}$ (MCN), $Li_{1.3}Mn^{3+}_{0.3}Cr^{3+}_{0.1}Ti_{0.3}O_{1.7}F_{0.3}$ (MCT) and $Li_{1.3}Mn^{2+}_{0.1}Co^{2+}_{0.1}Mn^{3+}_{0.1}Cr^{3+}_{0.1}Ti_{0.1}Nb_{0.2}O_{1.7}F_{0.3}$ (TM6 in the main text), TM6 shows a much larger capacity (307 mAh g^{-1}, Figure 2c) than either MCN (244 mAh g^{-1}, Figure S5h) or MCT (243 mAh g^{-1}, Figure S5i), suggesting that Cr^{3+} alone does not account for the improved capacity either.

We believe that this series of experiments confirms that the improvement in capacity in going from TM2, to TM4 and TM6 cannot be attributed to any direct or indirect effect of a specific TM (e.g. electronic structure or size) but only by the synergy of having them all together, which is what the entropic effect is.

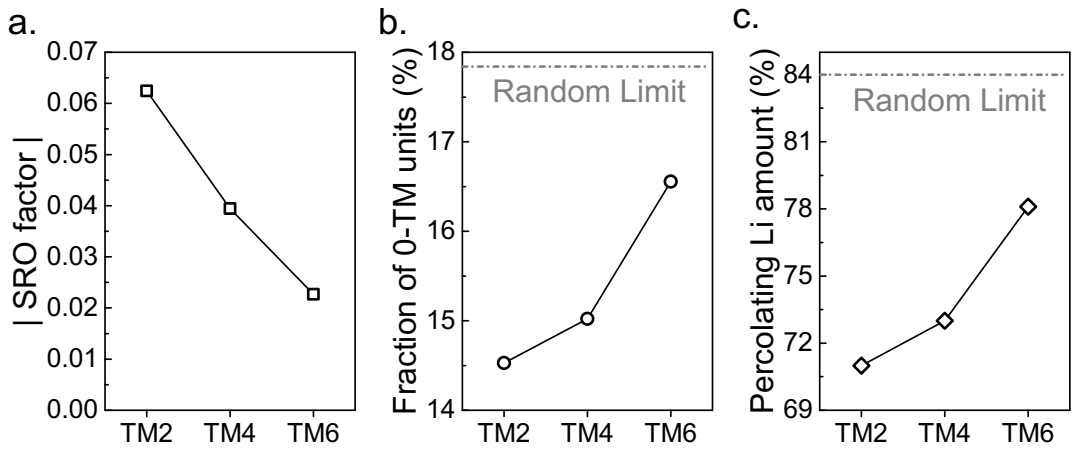

Figure S6 | Computational analyses of the SRO and Li percolation of the three compounds. **a.** Calculated Warren-Cowley SRO parameter (plotted in absolute value); b. Fraction of 0-TM tetrahedral units in the three compounds, and the value of random limit (infinite temperature) is marked by the grey dashed line. c. Amount of 0-TM-connected Li (percolating Li) per f.u. and comparison with random limit in the three compounds. All parameters are derived from Monte Carlo structures simulated at 1273K for TM2, TM4 and TM6**.** It can be clearly observed that the Warren-Cowley SRO parameter approaches zero (random limit, no SRO) as number of TM increases from TM2 to TM6. In consequence, the fraction of 0-TM units and the percolating Li amount increase from TM2 to TM6 monotonically.

Supplementary Note 3: Computational analysis of SRO and macroscopic Li percolation

We constructed a cluster expansion and combined that with Monte Carlo (MC) simulations to model SRO of DRX to the best accuracy we can achieve at this stage. We also run percolation analysis and evaluated the Cowley-Warren SRO parameters [6] using a cluster expansion constructed in the Li^{+}-Mn^{2+}-Mn^{3+}-Ti^{4+}-Nb^{5+}-Co^{2+}-Cr^{3+}-O^{2-}-F^{-} compositional space, with all the details listed in the methodology part. The MC and SRO analysis on TM2, TM4 and TM6 compounds (Figure S6) clearly show that the Warren Cowley SRO parameters get closer to zero (fully random) when the number of components increases (Figure S6a), indicating the mitigation of SRO. As a consequence, the fraction of 0-TM units and the total amount of percolating Li increases monotonically as number of TM species goes up, as shown in Figure S6b and S6c, respectively. Both results are consistent with our experimental observations.

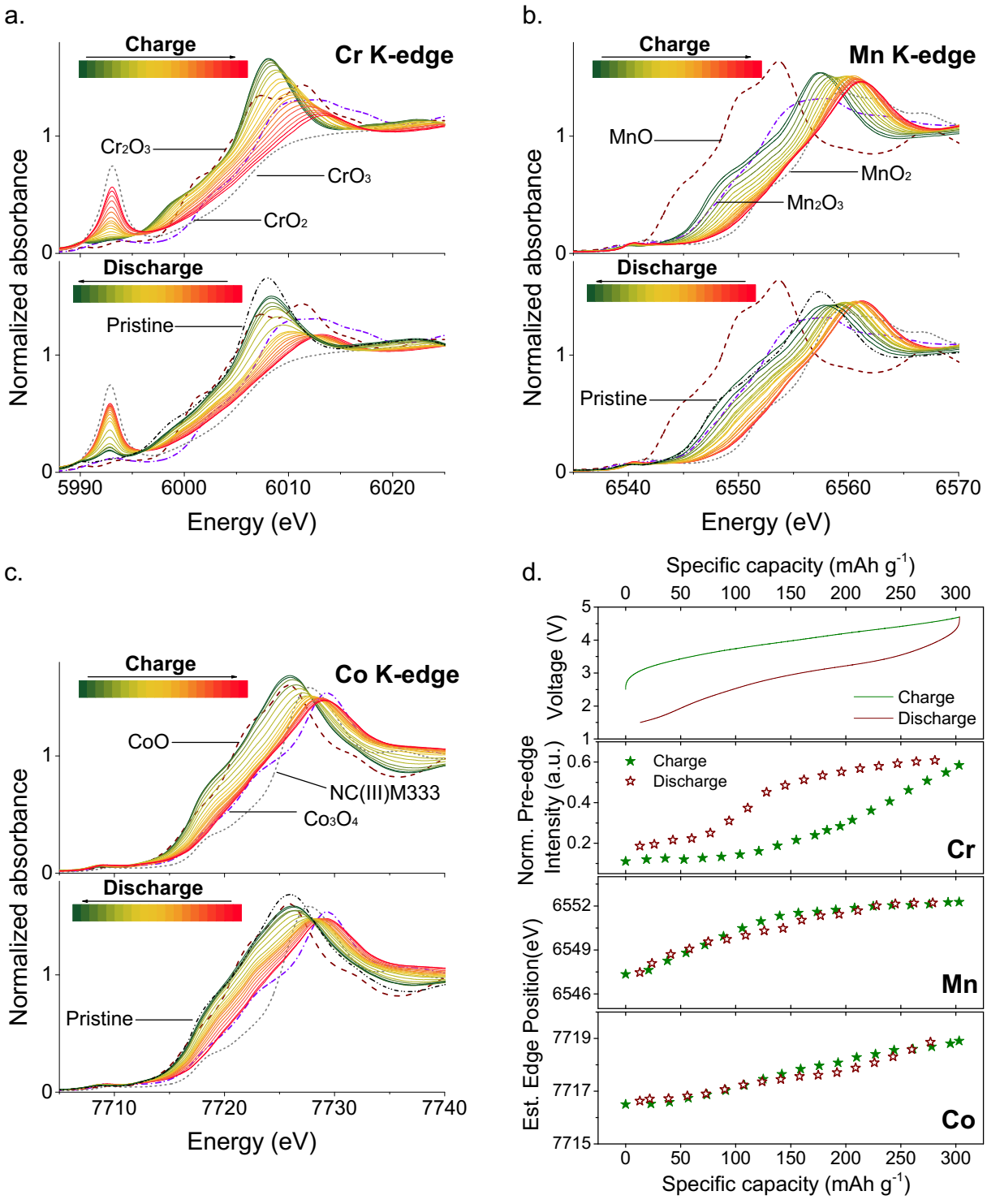

Figure S7 | TM redox behavior of TM6. XANES spectra at different states of charge from the first cycle at **a.** Cr K-edge, **b.** Mn K-edge, and **c.** Co K-edge acquired by *operando* XAS measurements. **d.** Voltage profile obtained from *operando* XAS measurement cycling at a rate of 16 mA g^{-1} and evolution of the oxidation states of the redox-active TMs, Cr, Mn, and Co, at

different states of charge from the first cycle. The *in-situ* cell was held at the top of charge for 30 min before discharging to obtain spectra at various edges. The oxidation state of Cr is estimated based on the normalized pre-edge intensity, whereas the oxidation states of Mn and Co are estimated by edge positions E(0.5) and E(0.4), respectively.

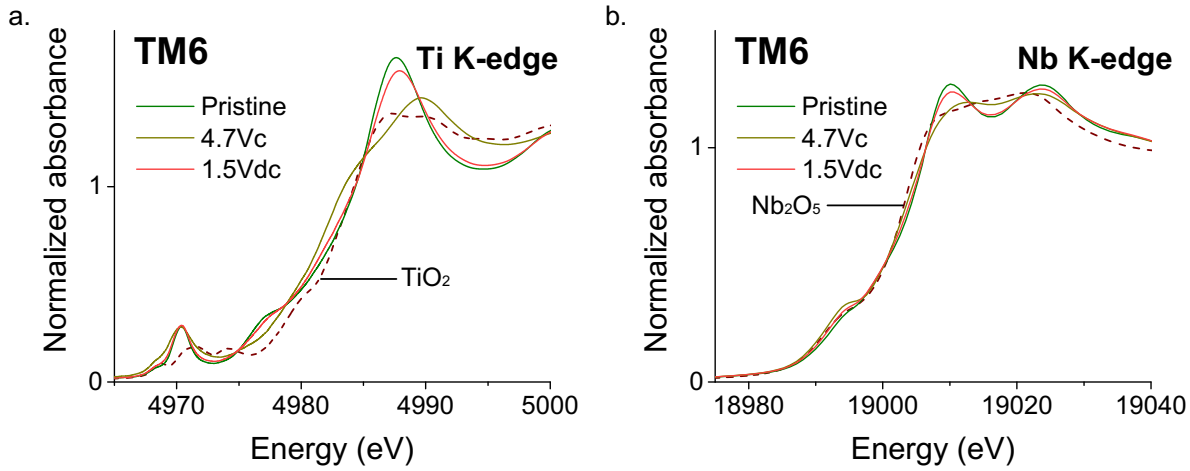

Figure S8 | Titanium (Ti) and Niobium (Nb) K-edge XANES spectra of TM6. *Ex-situ* **a.** Ti and **b.** Nb K-edge XANES spectra obtained from hXAS at pristine, top-of-charge (4.7 V), and end-of-discharge (1.5 V) states. TiO_2 and Nb_2O_5 references are also presented. The edge positions for both Ti and Nb remain unchanged at different states of charge and are close to that of the fully oxidized standards, indicating that Ti and Nb remain Ti^{4+} and Nb^{5+} and are redox inactive upon cycling.

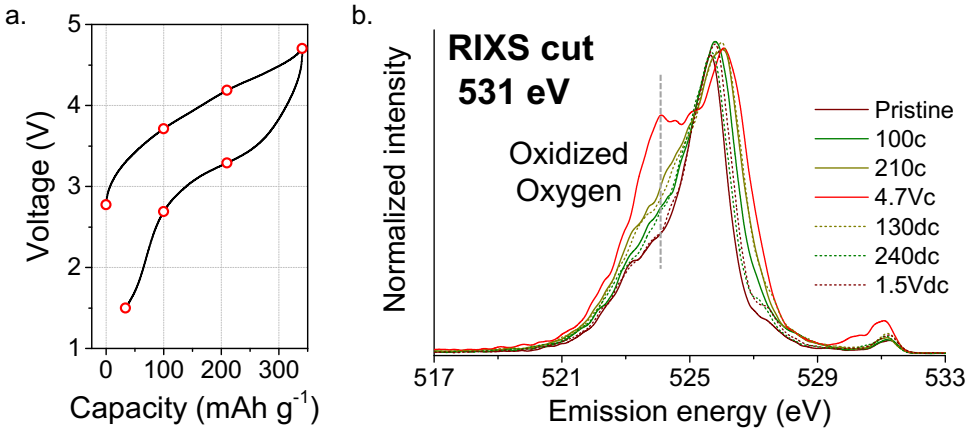

Figure S9 | Oxygen redox behavior of TM6. a. Voltage profile of the first cycle with seven states (red circles) selected for RIXS experiment, which are pristine; charged to 100 mAh g^{-1}, 210 mAh g^{-1}, and 4.7 V; charged to 4.7 V followed by discharging to 130 mAh g^{-1}, 240 mAh g^{-1}, and 1.5 V. **b.** RIXS spectra collected at the excitation energy of 531 eV. The dashed line denotes the position of the characteristic oxygen-oxidation feature, which is at ~524 eV emission energy. The emergence of the high intensity peak here indicates oxidized lattice oxygen; upon discharging, the intensity drops back to that of the pristine state, indicating a fairly reversible oxygen redox reaction.

Supplementary Note 4: Redox mechanism of TM6

The stepwise redox behavior of different TM redox centers in TM6 was probed by *operando* hXAS measurement. The XANES spectra at the Cr, Mn, and Co K-edges are shown in Figure S7a–c. The valences of Cr were estimated by the pre-edge intensity, whereas those of Mn and Co were estimated from the K-edge energies. The estimated evolution of the oxidation state of various redox-active TMs upon electrochemical cycling is shown in Figure S7d. During charging, Mn is oxidized first from Mn^{2+} to Mn^{3+} and further towards Mn^{4+}. The Co^{2+}/Co^{3+} oxidation occurs after 50 mAh g^{-1} and strongly overlaps with the Mn oxidation. The Cr^{3+}/Cr^{6+} oxidation starts after charging to more than 120 mAh g^{-1} and continues until the top of charge. At the top of charge, the percentage of Mn^{2+}/Mn^{4+} oxidation is estimated to be nearly 100%, whereas that of Cr^{3+}/Cr^{6+} oxidation and Co^{2+}/Co^{3+} oxidation are ~70% and ~67%, respectively. Upon discharge, all three metal K-edges shift back to their initial energy positions, indicating good reversibility of the metal redox. In total, the TM redox contributes ~175 mAh g^{-1} to the total capacity. Notably, during discharge, the order of reduction reactions does not exactly reverse that during charge. At the beginning of discharge, no obvious metal reduction is observed until the discharge capacity reaches ~40 mAh g^{-1}, when the Co^{3+}/Co^{2+} reduction begins. Mn and Cr reduction processes start almost simultaneously after the discharge capacity reaches ~120 mAh g^{-1} and are highly overlapped. Toward the end of discharge, the capacity is mainly from Mn^{3+}/Mn^{2+} reduction. Clearly, there is a voltage hysteresis for the Cr redox, as observed in other Li-ion cathode materials [4], presumably because Cr^{6+} migrates to tetrahedral sites during the charge process, making it difficult to be reduced during discharge. Nevertheless, the presence of multiple redox centers in TM6 mitigates the overall voltage hysteresis. Ti^{4+} and Nb^{5+} remain redox inactive during cycling, as observed in the *ex-situ* XANES spectra in Figure S8.

The lattice oxygen redox processes can be directly detected by the state-of-the-art *O-K* RIXS [7-18]. Compared with conventional *O-K* XAS that is dominated by the TM-O hybridization feature [19], RIXS could separate the different signal contributions and distinguish the signature of lattice oxygen redox. As discussed in previous *O-K* RIXS studies, most oxygen redox systems display a characteristic oxidized oxygen feature at an excitation energy of ~531 eV with an emission energy of ~524 eV in mapping. Therefore, RIXS spectra at the excitation energy of 531 eV can be used as a more direct spectral comparison of the evolution of the oxidized oxygen species. As demonstrated in Figure S9a, seven *ex-situ* samples at different states of charge from the first cycle

of TM6 were prepared: pristine; charged to 100 mAh g^{-1}, 210 mAh g^{-1}, and 4.7 V; and charged to 4.7 V followed by discharging to 130 mAh g^{-1}, 240 mAh g^{-1}, and 1.5 V. Their corresponding RIXS spectra at the excitation energy of 531 eV are presented in Figure S9b. The intensity of the ~524 eV (emission energy) signal is directly related to the lattice oxygen redox (marked by the grey dashed line). It can be observed that most of the intensity growth occurs between the charged to 210 mAh g^{-1} and the top-of-charge states, though there is a small amount of intensity growth before the charged to 210 mAh g^{-1} state. This observation is consistent with the hXAS finding that oxygen oxidation mainly occurs at high voltage, with small contributions in the low-voltage region. During discharge to 1.5 V, the intensity of the oxygen redox signal gradually decreases and is mostly recovered to that of the pristine state, indicating a good reversibility of the lattice-oxygen redox.

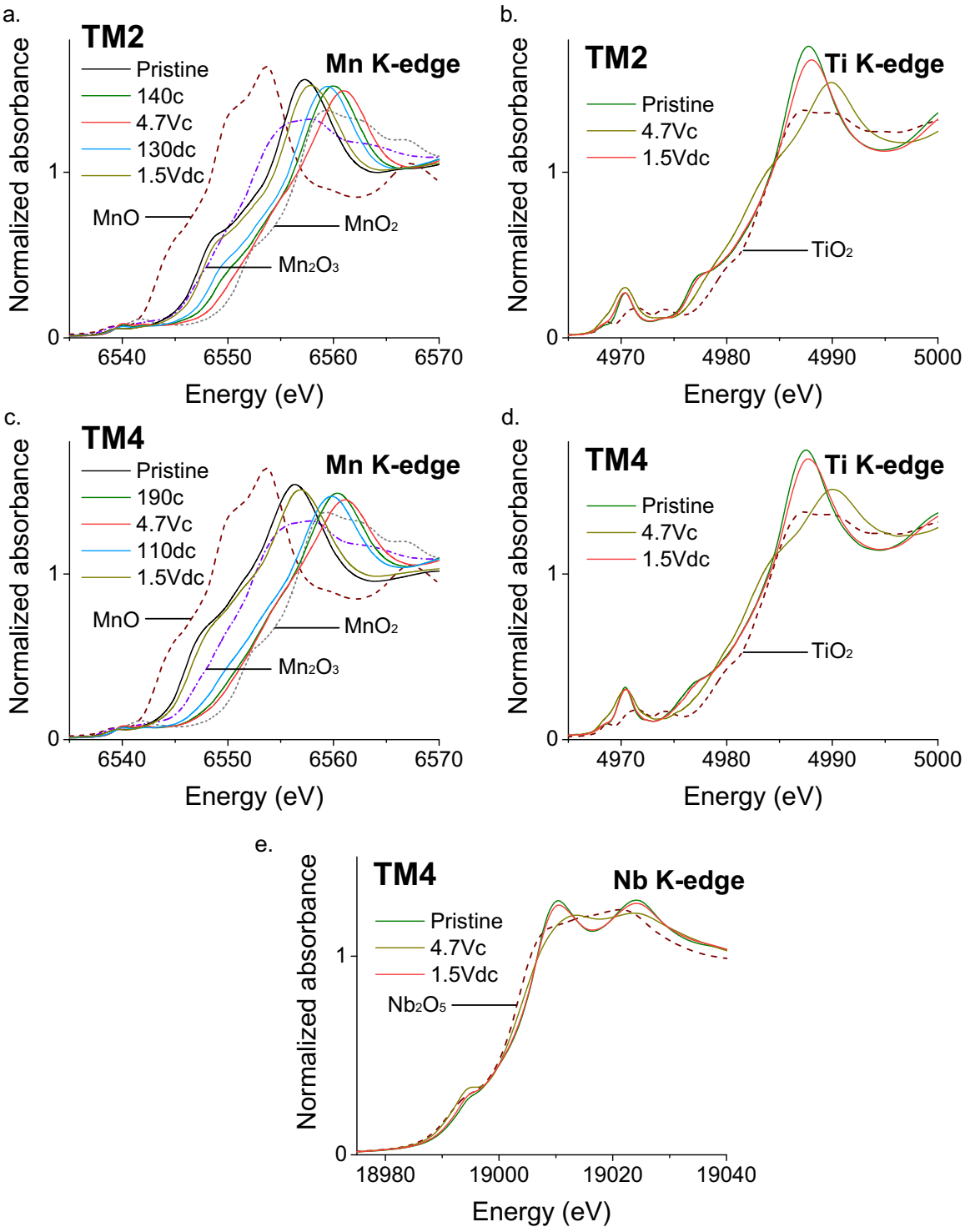

Figure S10 | TM redox behavior in TM2 and TM4. a. Mn K-edge XANES spectra of TM2 collected at five different states of charge from the first cycle: pristine; charged to 140 mAh g^{-1} and 4.7 V; and charged to 4.7 V followed by discharge to 130 mAh g^{-1} and 1.5 V. **b.** Ti XANES spectra of TM2 at pristine, top-of-charge (4.7 V), and end-of-discharge (1.5 V) states. **c.** Mn K-

edge XANES spectra of TM4 collected at five different states of charge from the first cycle: pristine; charged to 190 mAh g^{-1} and 4.7 V; and charged to 4.7 V followed by discharge to 110 mAh g^{-1} and 1.5 V. **d.** Ti and **e.** Nb XANES spectra of TM2 at pristine, top-of-charge (4.7 V), and end-of-discharge (1.5 V) states.

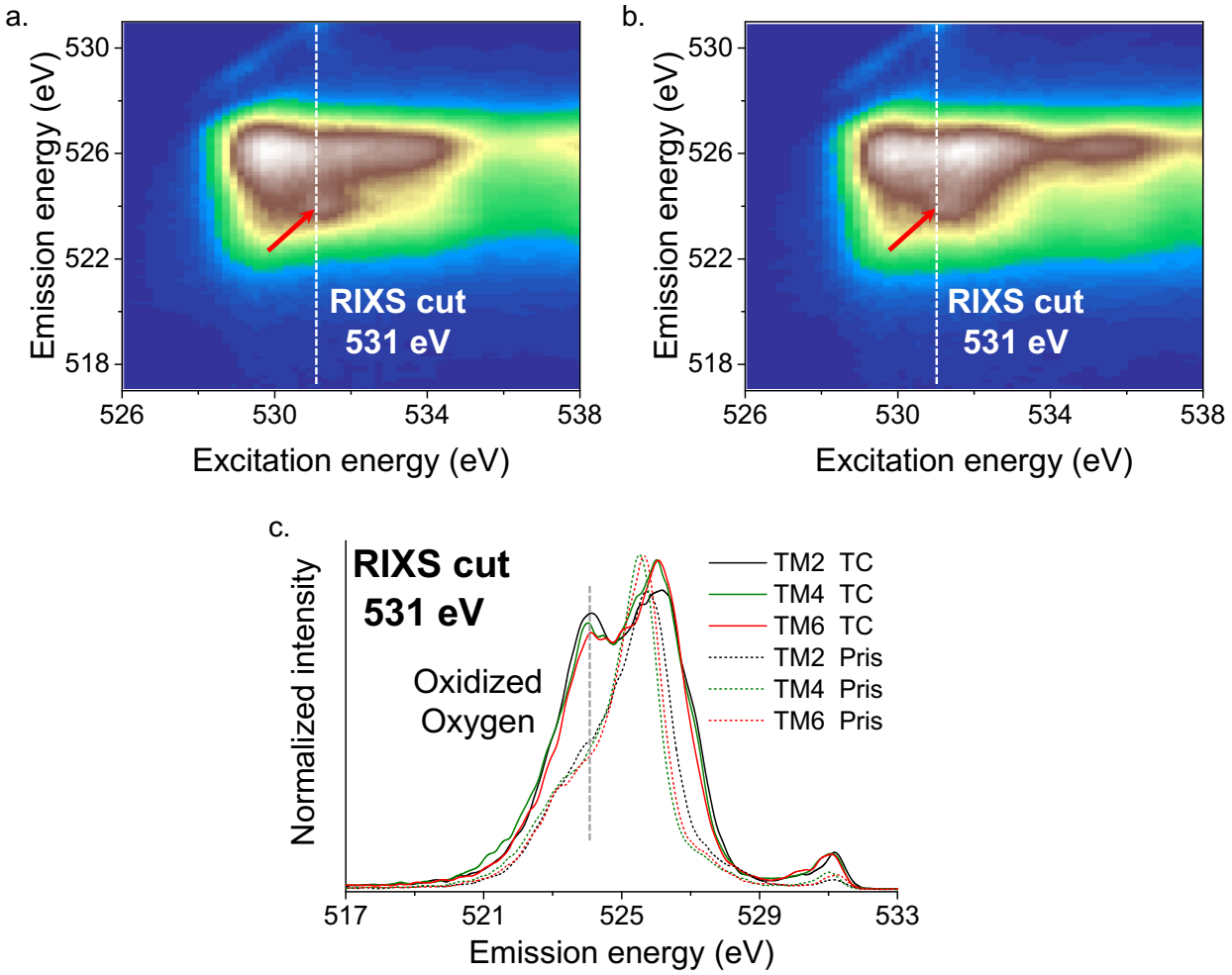

Figure S11 | RIXS map of **a.** TM2 and **b.** TM4 at top-of-charge state (4.7 V). The red arrows mark the oxidized oxygen feature. **c.** RIXS spectra collected at the excitation energy of 531 eV at pristine and the top-of-charge state on TM2, TM4, and TM6. The dashed grey line marks the position of the oxidized oxygen feature.

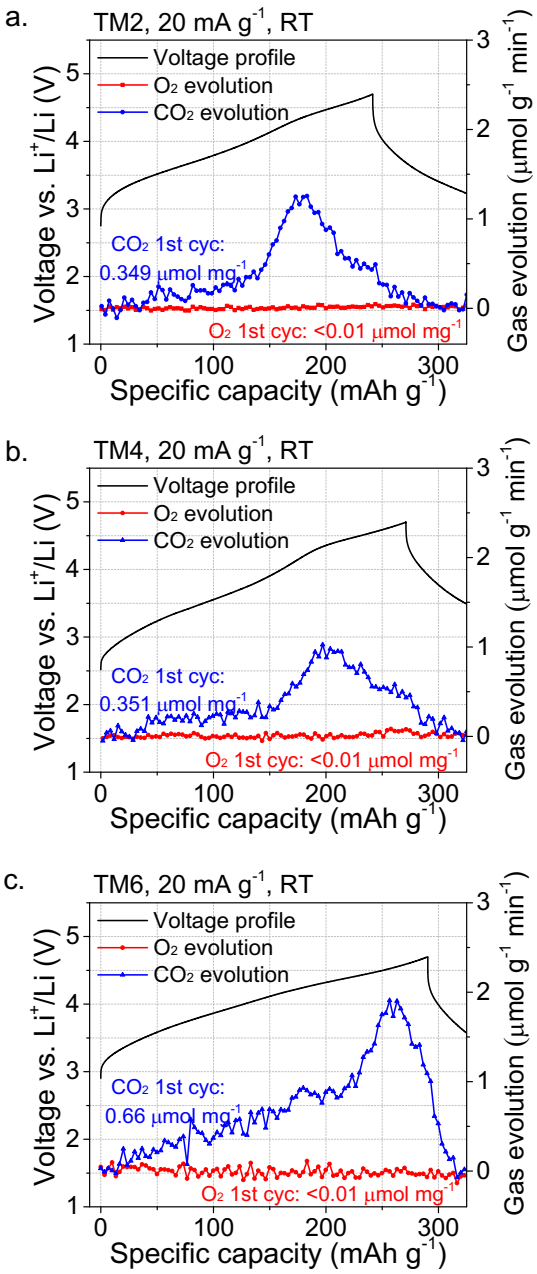

Figure S12 | Operando DEMS results for a. TM2, **b.** TM4, and **c.** TM6. The black solid lines, red dots, and blue triangles correspond to the voltage profiles, O_2 evolution, and CO_2 evolution, respectively. The amount of gas evolution is normalized based on the weight of the tested electrode. Irreversible oxygen evolution is negligible for all three materials upon cycling.

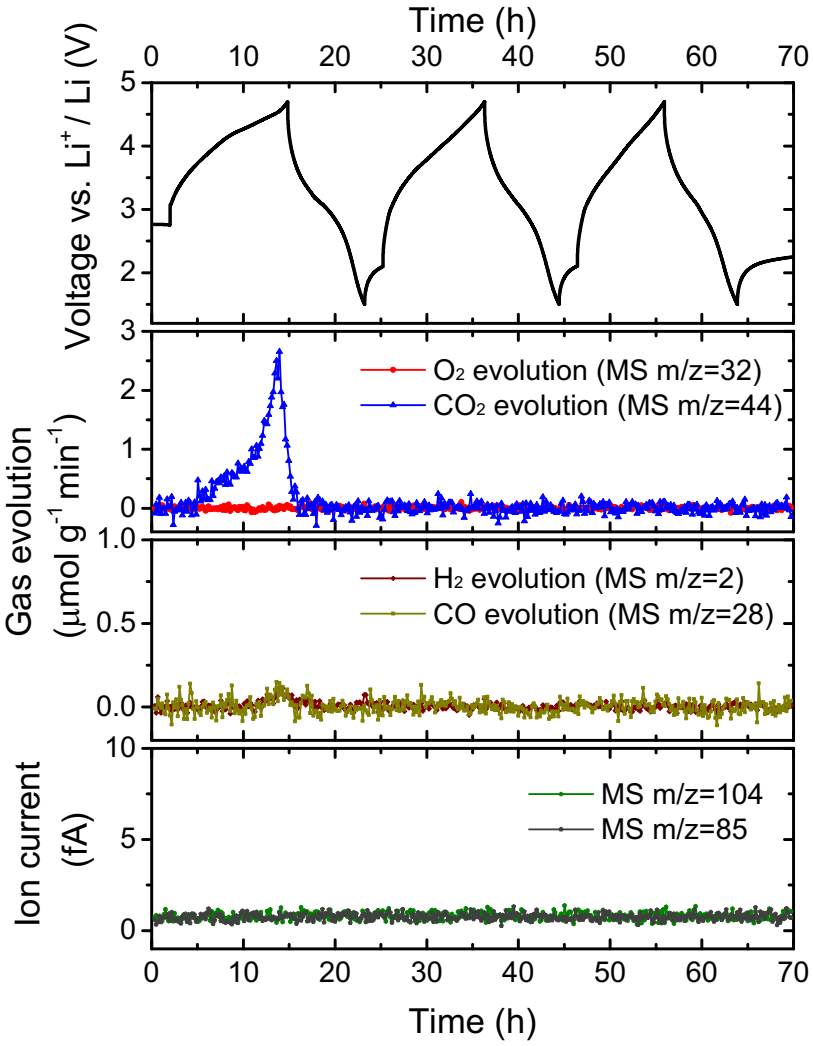

Figure S13 | Operando DEMS results for TM6 upon the first three cycles. The cell was cycled between 1.5 and 4.7 V at a rate of C/10, and the voltage profile is shown in the top panel. Gas evolution of O_2 (MS, m/z=32), CO_2 (MS, m/z=44), H_2 (MS, m/z=2), CO (MS, m/z=28), and POF_3 (MS, m/z=104 and m/z=85) [20] was measured and plotted in the lower panels. The amount of gas evolution is normalized based on the weight of the tested electrode. The evolution of H_2, CO_2, O_2, CO and POF_3 gas was monitored *in-situ* upon cycling. Negligible O_2 or POF_3 evolution is observed over the first three cycles, while certain amount of H_2, CO_2, and CO evolution is detected during the first cycle but is barely observable in the following cycles.

Supplementary Note 5: Redox mechanisms of TM2 and TM4 and comparison of oxygen redox in three materials

The redox behavior of TM2 and TM4 was investigated by combining *ex-situ* hXAS and RIXS, with hXAS to probe the TM redox behavior (Figure S10) and RIXS to detect lattice-oxygen redox(Figure S11). For TM2, the Mn K-edge spectra of the pristine; charged to 140 mAh g^{-1} (corresponding to the theoretical Mn^{3+}/Mn^{4+} redox capacity) and 4.7 V; and charged to 4.7 V followed by discharge to 130 mAh g^{-1} and 1.5 V states are presented in Figure S10a. Upon charging to 140 mAh g^{-1}, the Mn K-edge shifts from an energy close to Mn_2O_3 to that of MnO_2, indicating Mn^{3+}/Mn^{4+} oxidation. When further charged to 4.7 V, the Mn K-edge only shifts slightly to a higher energy and almost overlaps with that of the MnO_2 reference. This result suggests that Mn redox contributes little capacity in this region and that most of the capacity originates from lattice-oxygen oxidation, as supported by the strong oxygen oxidation signal in the *O-K* RIXS mapping (Figure S11a). Nearly all Mn is oxidized to Mn^{4+} at the top of charge. During discharge, Mn is gradually reduced to Mn^{3+}, with more reduction reactions occurring at low voltage, as indicated by the much smaller shift between the top-of-charge and discharged to 130 mAh g^{-1} states. At the end of discharge (1.5 V), the Mn K-edge returns to a similar position as that of the pristine materials, suggesting the good reversibility of the redox reaction. The shape of the Mn K-edge changes slightly because of the possible local structural rearrangement upon cycling.[21] The Ti K-edge position barely changes upon cycling, as observed in Figure S10b, which proves that Ti is redox inactive.

For TM4, Mn K-edge spectra were collected at five different states of charge: pristine; charged to 190 mAh g^{-1} (corresponding to the theoretical Mn redox capacity) and 4.7 V; and charged to 4.7 V followed by discharge to 110 mAh g^{-1} and 1.5 V, as shown in Figure S10c. When charged to 190 mAh g^{-1}, the Mn K-edge shifts from an energy in between those of MnO and Mn_2O_3 to that of MnO_2 and barely changed upon further charging to 4.7 V. This result suggests that the Mn redox dominates at low voltage and that Mn can be fully oxidized to Mn^{4+}, followed by oxygen oxidation contributing to the rest of the capacity. A clear lattice-oxygen-oxidation characteristic feature can be observed in the *O-K* RIXS mapping in Figure S11b. Upon discharge, the Mn K-edge reversibly shifts back to an energy close to its original position with only a small change in shape. Ti and Nb do not participate in the redox process, as observed in Figure S10d–e.

In Figure S11c, the *O-K* RIXS spectra at the excitation energy of 531 eV are compared between the pristine state and the top of charge for the TM2, TM4, and TM6 compounds. All three materials at the top of charge have significant oxygen oxidation features, as indicated by the grey dashed line in the figures. All three materials show negligible oxygen loss, as demonstrated from differential electrochemical mass spectrometer (DEMS) measurement, shown in Figure S12-13, which indicates good reversibility of oxygen redox.

Combined with the previous finding that most of the TM redox reactions are active and reversible in all three compounds, the oxygen redox behavior studies indicate that it is unlikely that the difference in the achieved capacity in the materials originates from a large difference in redox behavior.

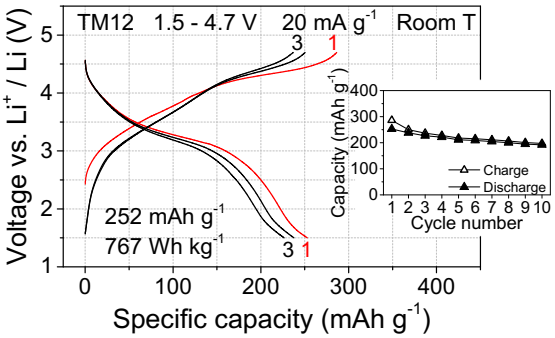

Figure S14 | Electrochemical performance of TM12. Voltage profiles and capacity retention of TM12 within the voltage window of 1.5–4.7 V at 20 mA g^{-1} and room temperature. Note that the composition of TM12 is not designed for an optimized electrochemical performance, instead, as a demonstration of the excellent structural compatibility of DRX structure. Despite the very diluted TM redox capacity (< 0.35 electron per f.u., corresponding to a capacity of <100 mAh g^{-1}) and the incorporation of some very heavy metal ions, such as Ta, and Sb, it still shows reasonably good specific capacity of 252 mAh g^{-1}.

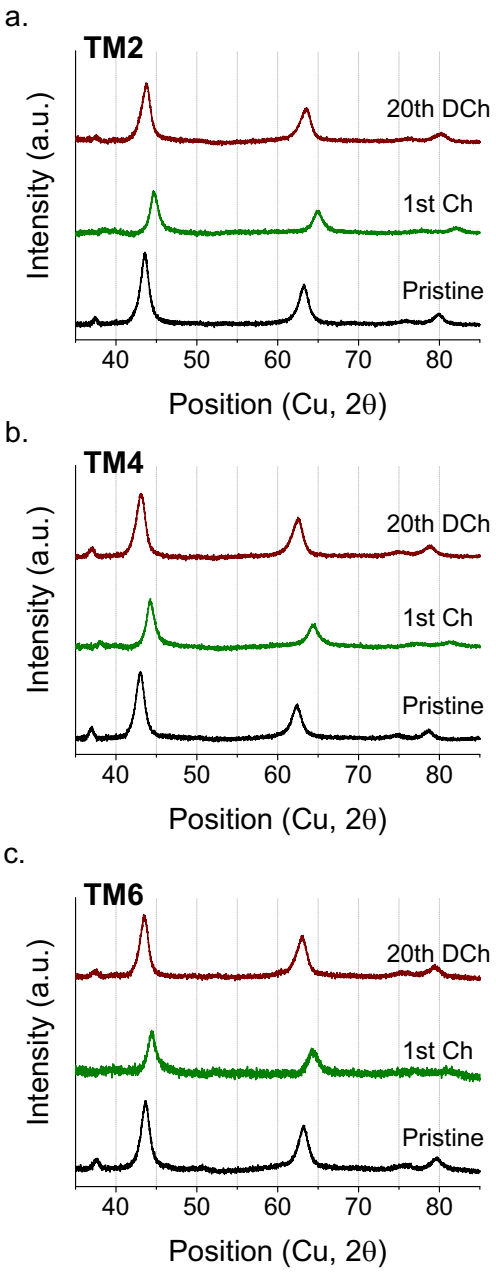

Figure S15 | Investigation of DRX structural stability upon cycling. *Ex-situ* XRD patterns collected on pristine electrodes, top-of-charge electrodes from the 1st cycle, and end-of-discharge electrodes from the 20th cycle for **a.** TM2, **b.** TM4, and **c.** TM6. No irreversible structural change can be observed in all three materials. The DRX lattice remains intact both at the top of charge and after extended cycles, indicating a good bulk structural stability without any major irreversible degradation.

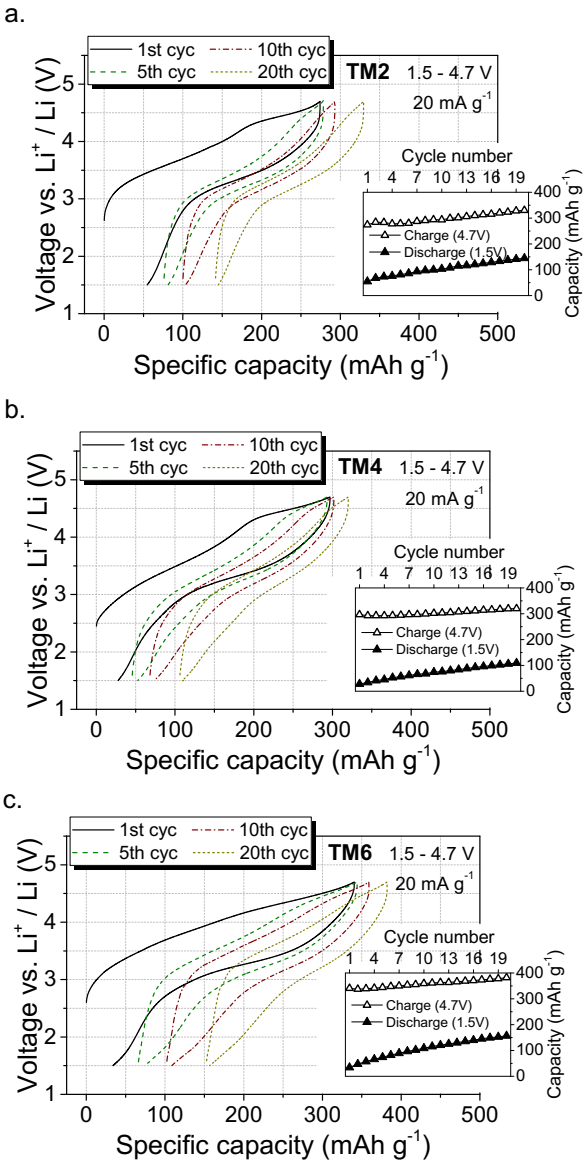

Figure S16 | Evaluation of the electrolyte-electrode reactivity. Voltage profiles of 1st, 5th, 10th and 20th cycles in **a.** TM2, **b.** TM4, and **c.** TM6, plotted in an "accumulated capacity" manner. The inset shows the accumulated capacity at the top of charge and the end of discharge in each cycle. The shifts for TM2, TM4 and TM6 after 20 cycles are 56 (from 274 mAh g^{-1} to 330 mAh g^{-1}), 23 (from 297 mAh g^{-1} to 320 mAh g^{-1}) and 41 mAh g^{-1} (from 341 mAh g^{-1} to 382 mAh g^{-1}), respectively, after 20 cycles.

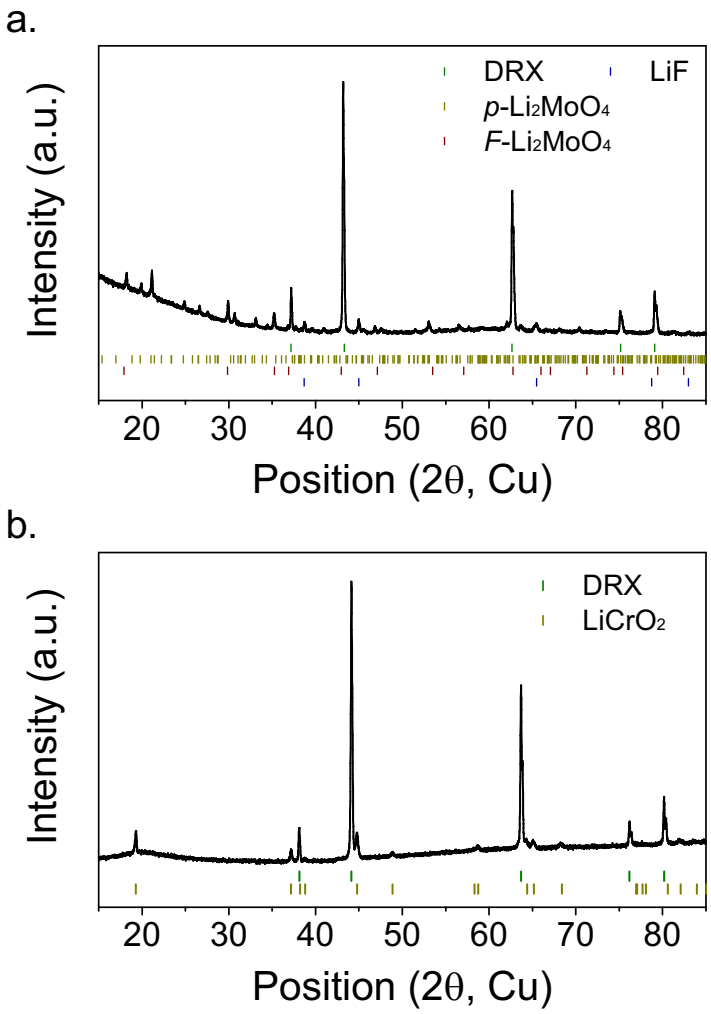

Figure S17 | HE DRX synthesis case study. Failed synthesis of the targeted compositions of **a.** $Li_{1.3}Mn^{2+}_{0.15}Mn^{3+}_{0.25}Ti_{0.05}Mo^{4+}_{0.1}Nb_{0.15}O_{1.7}F_{0.3}$ and **b.** $Li_{1.3}Co^{2+}_{0.2}Cr^{3+}_{0.2}Ti_{0.1}Nb_{0.2}O_{1.7}F_{0.3}$.

Supplementary Note 6: Case study of HE DRX synthesis

In the design of HE DRX materials, two compatibility issues, redox compatibility and phase compatibility, should be considered. Figure S17 shows two failed synthesis attempts of HE DRX cathodes due to incompatibility. Figure S17a shows a failed experiment with the target composition of $Li_{1.3}Mn^{2+}_{0.15}Mn^{3+}_{0.25}Ti_{0.05}Mo^{4+}_{0.1}Nb_{0.15}O_{1.7}F_{0.3}$. Several impurity phases were detected in the XRD pattern, including two different Li_2MoO_4 phases and LiF. Here, Mn^{3+} and Mo^{4+} are redox incompatible, i.e., when they coexist, Mn^{3+} will be reduced to Mn^{2+} while Mo^{4+} is oxidized to Mo^{6+}, leading to the synthesis failure. Figure S17b shows another failed experiment due to chemical incompatibility with the target composition of $Li_{1.3}Co^{2+}_{0.2}Cr^{3+}_{0.2}Ti_{0.1}Nb_{0.2}O_{1.7}F_{0.3}$. The Cr^{3+} ion strongly prefers a perfect octahedral coordination environment; therefore, if its concentration is larger than the tolerance limit of the DRX structure, a layered $LiCrO_2$ impurity starts to appear, resulting in the synthesis failure. These two cases motivated us to study the redox compatibility and phase compatibility through computational screening to facilitate the future design of HE DRX cathodes.

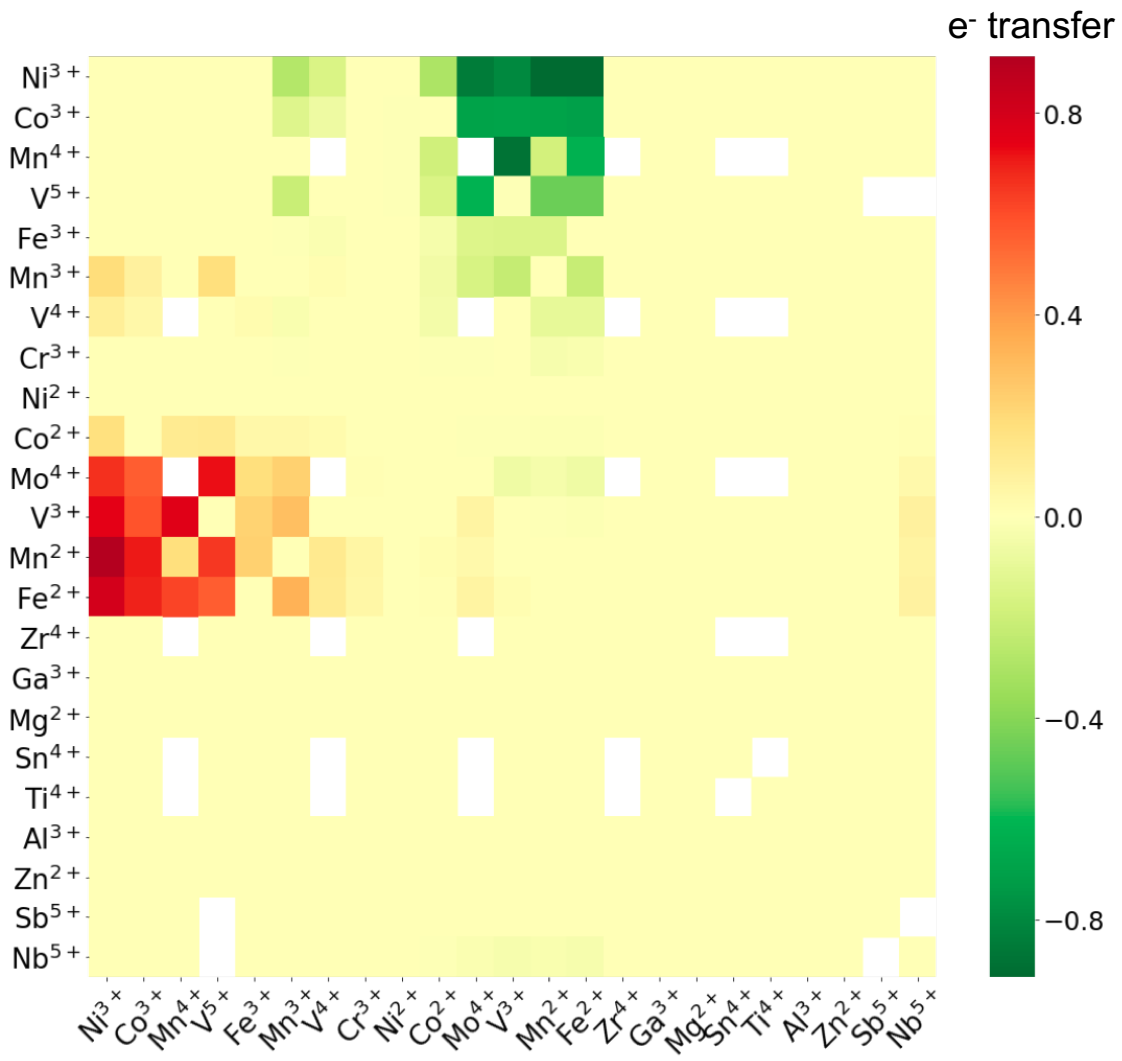

Figure S18 | Redox compatibility analysis of different TM species in a DRX lattice. Red regions indicate redox-incompatible pairs in which the elements from the horizontal axis will oxidize those from the vertical axis. Green regions indicate redox-incompatible pairs with an opposite direction of charge transfer. Yellow regions denote redox-compatible pairs. All the redox-incompatible TM pairs are colored grey in Figure 4c.

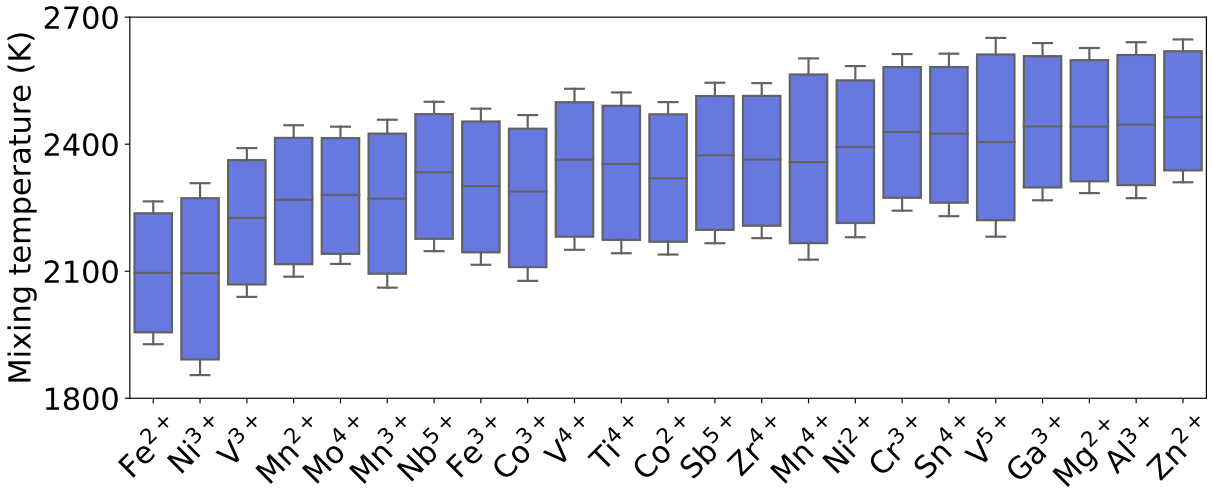

Figure S19 | Calculated distribution of mixing temperatures of various metal species in HE DRX compounds.

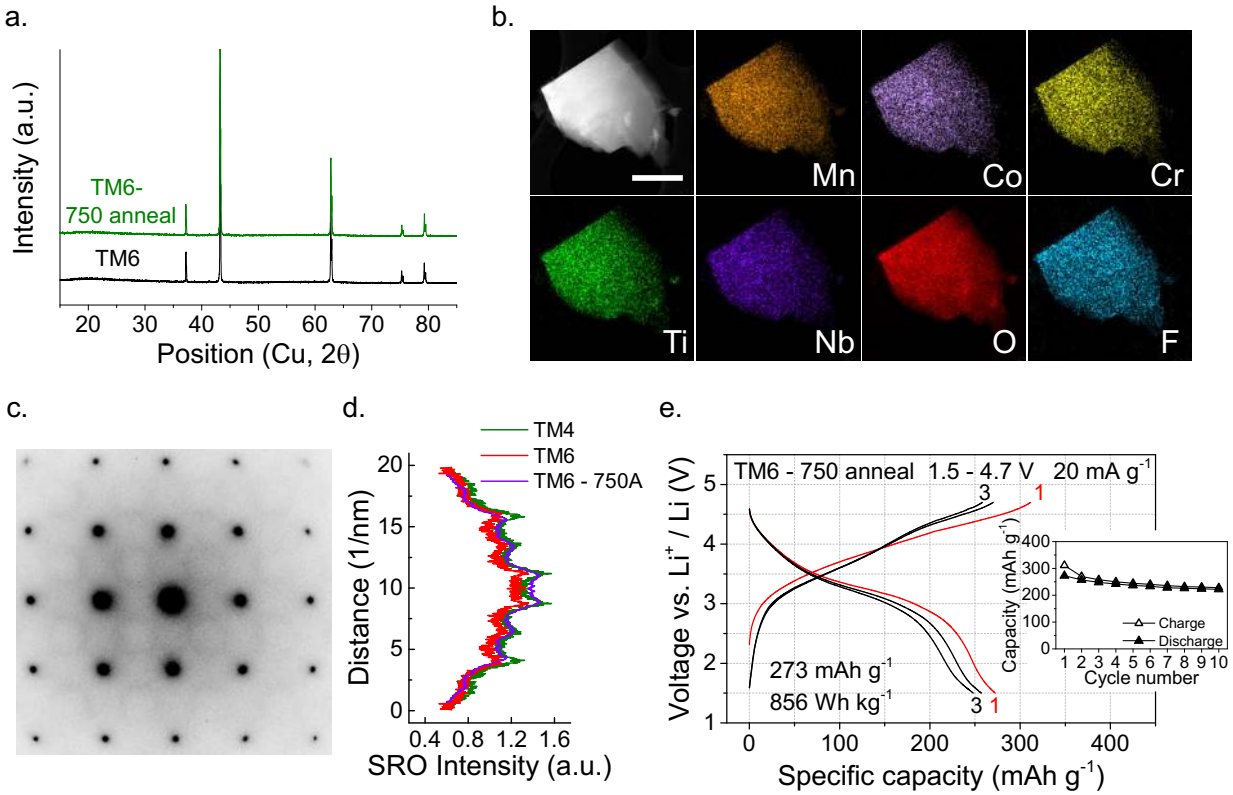

Figure S20 | Evaluation of the effect of synthesis condition on the SRO in TM6. a. XRD patterns of as-synthesized TM6 and 750 ℃ annealed (10 hours) TM6. Neither impurity peaks arising nor obvious peak position shift can be observed after annealing treatment, indicating the maintenance of the same LRO. **b.** STEM/EDS mappings of elemental distribution in a particle of 750-annealed TM6 (Scale bar: 400nm). The results suggest all the elements are uniformly distributed with no phase segregation in the particle. **c.** ED pattern collected on 750-annealed TM6 along the [100] zone axis and **d.** The SRO intensity profiles from as-synthesized TM4, as-synthesized TM6 and 750-annealed TM6 are compared. The 750-annealed TM6 sample presents increased SRO intensity compared to that in as-synthesized TM6, comparable to that in TM4. **e.** Voltage profiles and capacity retention of 750-annealed TM6 within the voltage window of 1.5–4.7 V at 20 mA g^{-1} and room temperature.

Supplementary Note 7: Evaluation of the effect of synthesis condition on the SRO in TM6

The SRO in DRX is a function of synthesis temperature, and in general SRO tends to decrease when increasing the temperature. As a demonstration of this effect, we annealed the as-synthesized TM6 at 750 ℃ for 10 hours after the sintering at 1000 ℃ to introduce a certain degree of SRO and investigate its influence on the electrochemical performance (Figure S20). Figure S20a shows the XRD patterns of the as-synthesized TM6 (from 1000 ℃, bottom, black curve) and the 750℃-re-annealed TM6 (top, green curve). No impurity peaks or peak shifting shows up in XRD after re-annealing, suggesting no long-range order change during re-annealing. The EDS mapping (Figure S20b) furthermore suggests a homogenous distribution of all the elements indicating no phase segregation after the re-annealing treatment. We took TEM electron diffraction (ED) on the re-annealed TM6 to investigate any change in SRO after the treatment (Figure S20c). The SRO intensity profiles of the as-synthesized TM4, the as-synthesized TM6 and the 750℃-re-annealed TM6 are compared in Figure S20d. Re-annealing at 750℃ leads to an increased SRO intensity in TM6, which is now as high as that observed in the as-synthesized TM4. Consistent with our conjecture, relating SRO to a degradation of performance, the electrochemical capacity also decreases in the re-annealed TM6 (Figure S20e), accompanying the increased SRO. Specifically, the re-annealed TM6 delivers a smaller capacity (specific energy) of 273 mAh g^{-1} (856 Wh kg^{-1}) than that of the as-synthesized TM6 (307 mAh g^{-1}, 955 Wh kg^{-1}).

As a final note, all the materials presented in the main text were synthesized using the same solid-state method from between 1000℃ and 1050℃. Therefore, the influence of synthesis conditions on SRO in the present study is minimal.

Table S1 | Target versus measured atomic ratios of the as-synthesized materials.

Materials	Target atomic ratio (Li : Mn : Co : Cr : Ti : Nb : F)	Measured ratio (Li : Mn : Co : Cr : Ti : Nb : F)
TM2	1.3 : 0.4 : 0 : 0 : 0.3 : 0 : 0.3	1.267 : 0.414 : 0 : 0 : 0.302 : 0 : 0.216
TM4	1.3 : 0.4 : 0 : 0 : 0.1 : 0.2 : 0.3	1.279 : 0.412 : 0 : 0 : 0.103 : 0.197 : 0.226
TM6	1.3 : 0.2 : 0.1 : 0.1 : 0.1 : 0.2 : 0.3	1.271 : 0.21 : 0.101 : 0.113 : 0.105 : 0.186 : 0.219

Note that while the measured metal ratios are close to the target, the detected fluorine contents in all three materials are slightly lower than expected. This may originate from several factors: (1) The loss of F-precursors (i.e. LiF) during high temperature synthesis. However, such loss is expected to be minimal given the close-to-expected Li contents in all materials. (2) Partial dissolution of the as-synthesized materials in aqueous acids prior to elemental analysis because of the low solubility of oxyfluorides. (3) The generation of HF gas which may happen during dissolution, causing F loss before the measurement. (2) and (3) together are likely to cause an under-estimation of the F content.

Table S2 | Competing phases generated by phase diagram analyses.

Type*	Competing phases
Elemental metals and intermetallics	Co Ni Mo Sn Sb CoSn Co_3Mo CoSb Ni_5Sb_2 Ni_3Sn Ni_3Sn_2 Ni_3Mo Ni_4Mo NiSb ZnNi
Metal Oxides/fluorides	MgO MgF_2 V_2O_3 MnO FeO Fe_3O_4 CoO NiO ZnO ZrO_2 MoO_2 SnO SnO_2 Sb_2O_3
Li-Metal Oxides	$LiAlO_2$ $LiAl_5O_8$ Li_2TiO_3 $LiVO_2$ Li_3VO_4 $LiCrO_2$ Li_3CrO_4 Li_2MnO_3 $LiMnO_2$ $LiFeO_2$ Li_2FeO_3 $LiCoO_2$ Li_2CoO_3 $LiNiO_2$ Li_2NiO_3 $LiGaO_2$ $LiGa_5O_8$ Li_2ZrO_3 Li_3NbO_4 $LiNbO_3$ Li_2MoO_3 Li_3MoO_4 Li_4MoO_5 Li_2MoO_4 $Li(MoO_2)_2$ Li_2SnO_3 Li_3SbO_4 $LiSbO_2$ $Li_2Sb_4O_7$ $LiSbO_3$
Metal-Metal Oxides	Mg_2NiO_3 $Mg(SbO_2)_2$ $Mg_4Nb_2O_9$ Mg_2TiO_4 $MgVO_3$ Mg_2SnO_4 $Mg(GaO_2)_2$ $MgAl_2O_4$ $MgCr_2O_4$ $Mg(FeO_2)_2$ $MgTiO_3$ Al_2FeO_4 Al_2CoO_4 $MnAl_2O_4$ Al_2ZnO_4 $Ti(FeO_2)_2$ $TiCoO_3$ $TiNiO_3$ $TiMnO_3$ $TiMn_2O_4$ $V(CoO_2)_2$ MnV_2O_4 $MnVO_3$ $VFeO_3$ Cr_2FeO_4 Cr_2CoO_4 Cr_2NiO_4 $MnCr_2O_4$ $ZnCr_2O_4$ $Mn(FeO_2)_2$ $Mn(SbO_2)_2$ Mn_2SnO_4 $Mn(GaO_2)_2$ $MnSnO_3$ Fe_2CoO_4 $Fe(SbO_2)_2$ $Zn(FeO_2)_2$ Co_2SnO_4 Ga_2CoO_4 $Ni(SbO_2)_2$ Ga_2NiO_4 $Zn(GaO_2)_2$
Li-Metal-Metal Oxides	$Li_3Mg_2SbO_6$ $Li_2MgSn_3O_8$ $Li_2Ti_3CoO_8$ $Li_2Ti_3NiO_8$ $Li_2Ti_3FeO_8$ $Li_2Ti_3ZnO_8$ $Li_2NbV_3O_8$ $Li_2V_3SnO_8$ $Li_2Cr_3SbO_8$ $LiCrSnO_4$ $LiMnNbO_4$ $LiMnSbO_4$ $Li_2MnSn_3O_8$ $Li_3Fe_4SbO_8$ $LiNbFeO_4$ $Li_2Fe_3SbO_8$ $LiFeSbO_4$ $LiCoSbO_4$ $LiNiSbO_4$ $Li_2ZnSn_3O_8$ $LiGaSnO_4$
Competing phases with > 2 metal elements	$Li_3MnFeNiO_6$

* The term "metal" in table denotes non-Li metal species.

Supplementary References

1 Lee, J. *et al.* Mitigating oxygen loss to improve the cycling performance of high capacity cation-disordered cathode materials. *Nature communications* **8**, 981 (2017).

2 Lun, Z. *et al.* Improved Cycling Performance of Li-Excess Cation-Disordered Cathode Materials upon Fluorine Substitution. *Advanced Energy Materials* **9**, 1802959, doi:doi:10.1002/aenm.201802959 (2019).

3 Richards, W. D., Dacek, S. T., Kitchaev, D. A. & Ceder, G. Fluorination of Lithium-Excess Transition Metal Oxide Cathode Materials. *Advanced Energy Materials* **8**, 1701533, doi:doi:10.1002/aenm.201701533 (2018).

4 Lyu, Y. *et al.* Probing Reversible Multielectron Transfer and Structure Evolution of Li1.2Cr0.4Mn0.4O2 Cathode Material for Li-Ion Batteries in a Voltage Range of 1.0–4.8 V. *Chemistry of Materials* **27**, 5238-5252, doi:10.1021/acs.chemmater.5b01362 (2015).

5 Wang, W. *et al.* Synthesis and electrochemical properties of Li1.3Nb0.3Cr0.4O2 as a high-capacity cathode material for rechargeable lithium batteries. *Chemical Communications* **54**, 13809-13812, doi:10.1039/C8CC07660J (2018).

6 Cowley, J. M. X-Ray Measurement of Order in Single Crystals of Cu3Au. *Journal of Applied Physics* **21**, 24-30, doi:10.1063/1.1699415 (1950).

7 Gent, W. E. *et al.* Coupling between oxygen redox and cation migration explains unusual electrochemistry in lithium-rich layered oxides. *Nat Commun* **8**, 2091, doi:10.1038/s41467-017-02041-x (2017).

8 Qiao, R. *et al.* Transition-metal redox evolution in LiNi 0.5 Mn 0.3 Co 0.2 O 2 electrodes at high potentials. *J Power Sources* **360**, 294-300, doi:10.1016/j.jpowsour.2017.06.009 (2017).

9 Xu, J. *et al.* Elucidating anionic oxygen activity in lithium-rich layered oxides. *Nat Commun* **9**, 947, doi:10.1038/s41467-018-03403-9 (2018).

10 Yang, W. & Devereaux, T. P. Anionic and cationic redox and interfaces in batteries: Advances from soft X-ray absorption spectroscopy to resonant inelastic scattering. *J Power Sources* **389**, 188-197, doi:10.1016/j.jpowsour.2018.04.018 (2018).

11 Zhuo, Z. *et al.* Spectroscopic Signature of Oxidized Oxygen States in Peroxides. *J Phys Chem Lett* **9**, 6378-6384, doi:10.1021/acs.jpclett.8b02757 (2018).

12 Dai, K. *et al.* High Reversibility of Lattice Oxygen Redox Quantified by Direct Bulk Probes of Both Anionic and Cationic Redox Reactions. *Joule* **3**, 518-541, doi:10.1016/j.joule.2018.11.014 (2019).

13 Lebens-Higgins, Z. W. *et al.* Distinction between Intrinsic and X-ray-Induced Oxidized Oxygen States in Li-Rich 3d Layered Oxides and LiAlO2. *J Phys Chem C* **123**, 13201-13207, doi:10.1021/acs.jpcc.9b01298 (2019).

14 Li, N. *et al.* Unraveling the Cationic and Anionic Redox Reactions in a Conventional Layered Oxide Cathode. *ACS Energy Letters* **4**, 2836-2842, doi:10.1021/acsenergylett.9b02147 (2019).

15 Wu, J. *et al.* Fingerprint Oxygen Redox Reactions in Batteries through High-Efficiency Mapping of Resonant Inelastic X-ray Scattering. *Condensed Matter* **4**, 5, doi:10.3390/condmat4010005 (2019).

16 Zhao, E. *et al.* Stabilizing the Oxygen Lattice and Reversible Oxygen Redox Chemistry through Structural Dimensionality in Lithium-Rich Cathode Oxides. *Angew Chem Int Ed Engl* **58**, 4323-4327, doi:10.1002/anie.201900444 (2019).

17 Dissociate lattice oxygen redox reactions from capacity and voltage drops of battery electrodes. *SCIENCE ADVANCES* **6**, eaaw3871, doi:10.1126/sciadv.aaw3871 (2020).
18 Lee, G. H. *et al.* Reversible Anionic Redox Activities in Conventional LiNi1/3Co1/3Mn1/3O2 Cathodes. *Angew Chem Int Ed Engl*, doi:10.1002/anie.202001349 (2020).
19 Ruimin, Q. *et al. Deciphering the Oxygen Absorption Pre-Edge: Universal Map of Transition Metal Redox Potentials in Batteries*. (2019).
20 Breitung, B. *et al.* Gassing Behavior of High-Entropy Oxide Anode and Oxyfluoride Cathode Probed Using Differential Electrochemical Mass Spectrometry. *Batteries & Supercaps* **3**, 361-369, doi:10.1002/batt.202000010 (2020).
21 Manceau, A., Marcus, M. A. & Grangeon, S. Determination of Mn valence states in mixed-valent manganates by XANES spectroscopy. *American Mineralogist* **97**, 816-827 (2012).